Generation of nanosecond wide pulses for the surface detector test system of the Pierre Auger Observatory

Masterarbeit
zur Erlangung des akademischen Grades
Master of Science
(M. Sc.)

der Universität Siegen

Naturwissenschaftlich
Technische Fakultät

Department Physik

vorgelegt von
Frederik Hermann Lauber
July 2015

Contents

List of Figures

List of Tables

1 Introduction

> For my part I know nothing with any certainty, but the sight of the stars makes me dream.
>
> *Vincent Van Gogh*

Earth is hit by a steady flux of highly energetic particles.

One experiment, which investigates these cosmic particles, is the Pierre Auger Observatory in the Pampa Amarilla in Argentina. Within the next years a major part of the electronics deployed in this experiment will be replaced with upgraded versions. Due to the number of components to be replaced, an automatic test system for the electronics is necessary.
This system is the Tank Simulator (TS) and is developed by the astroparticle physics group of Siegen University. In the future the TS will be used to emulate the analog output of a surface detector station in order to provide a test environment for the upgraded electronics. Two solutions for the analog output of the TS are under development. The test and the evaluation of one solution is the subject of this thesis.

The following chapter gives an introduction to cosmic rays, their properties, and possible origins. This is followed by a description of the Pierre Auger Observatory and its planned upgrades in chapter 3. The generation and the properties of the analog outputs of the TS are described in chapter 4. Chapter 5 describes the data acquisition system of the measurement setup used to test the analog pulse generation. The analysis of the data obtained is described in chapter 6. A summary of the results of the analysis is given in chapter 7.

2 Cosmic Rays

Earth is hit by a steady flux of charged particles from outer space. They originate from the sun as well as from sources beyond the solar system. These particles are called cosmic particles or cosmic rays.

2.1. Energy Spectrum

Up to now, cosmic rays with an energy of up to 3×10^{20} eV [Bir+93] have been measured. The particle flux decreases with increasing energy. The energy spectrum of cosmic rays can be described by a power law

$$\frac{dF}{dE} \propto E^{-\gamma} \tag{2.1}$$

where F is the flux and E is the energy of the cosmic rays. The variable γ is called the spectral index. The energy spectrum is depicted in Figure 2.1. The spectral index changes rapidly in multiple positions of the energy spectrum. From lower energy to higher energy, these positions are called the knee, the 2nd knee, and the ankle. The spectral index values between these positions are listed in Table 2.1. The origin of these features of the spectrum is unknown and under scientific investigation. The most common explanations are an acceleration limit at the source of cosmic particles for different elements and a shift from galactic sources to extra galactic sources [BEH09].

For the acceleration of cosmic particles, two classes of models exist, the bottom-up and the top-down class. Every acceleration model which accelerates a particle from rest to cosmic particle energy is part of the bottom-up class. If the particle is not accelerated but created at cosmic particle energy, the model is part of the top-down class. At the time, current experimental results favor the bottom-up class models [Set11]. Any cosmic particle with an energy above 10^{18} eV is called an Ultra-High-Energy Cosmic Ray (UHECR).

E (eV)		1st knee $\approx 3 \times 10^{15}$		2nd knee $\approx 3 \times 10^{17}$		ankle $\approx 3 \times 10^{18}$	
spectral index γ	2.7		3.0		3.3		2.6

Tab. 2.1.: Values of the spectral index in different regions of the cosmic ray energy spectrum.

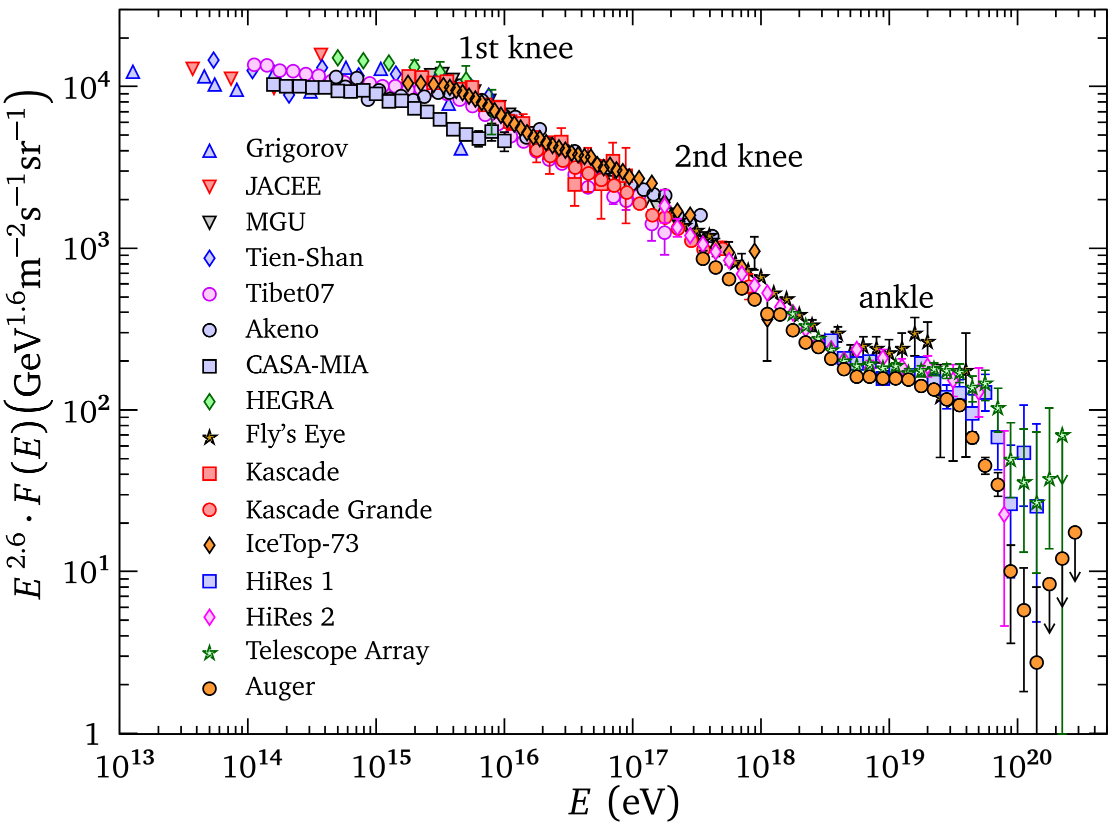

Fig. 2.1.: Cosmic ray particle flux against cosmic ray energy.
The flux of cosmic particles on the y-axis, range $1\,\mathrm{GeV}^{1.6}\mathrm{m}^{-2}\mathrm{s}^{-1}\mathrm{sr}^{-1}$ to approximately $2 \times 10^4\,\mathrm{GeV}^{1.6}\mathrm{m}^{-2}\mathrm{s}^{-1}\mathrm{sr}^{-1}$, is plotted against the energy per nucleus at 10^{13} eV/nucleus up to 10^{21} eV/nucleus on the x-axis. The flux was scaled by $E^{2.6}$ to make the features of the energy spectrum more distinct to the human eye. Both scales are logarithmic. Data from multiple experiments, listed in the legend and indicated by different data point styles, have been combined. The data points follow the power law given in Equation 2.1. The first and second knee as well as the ankle are labeled [Oli+14].

2.2. Mass Composition

Of cosmic ray particles, 2 % are electrons, while 98 % are nuclei of different masses. While the flux of these nuclei depends on the energies of the cosmic particles as seen in Figure 2.3, the ratio of nuclei is approximately constant for cosmic particle energies below 10^{14} eV. The largest fraction of 85 % are hydrogen nuclei followed by 12 % of helium nuclei. The remaining 3 % are a combination of other elements [BEH09]. The relative mass composition of cosmic ray nuclei at a cosmic ray particle energy of 10^9 eV per nucleon as well as the relative abundance of the elements in the solar system are depicted in Figure 2.2. The mass compositions of the solar system and cosmic rays match well, but some clear differences can be seen. These differences are used to investigate the mechanisms behind the cosmic ray production as well as the propagation of cosmic rays through interstellar space. E. g. lithium, beryllium, and boron are more abundant in cosmic rays than in the solar system. This is attributed to interstellar spallation processes between the interstellar matter and cosmic rays.

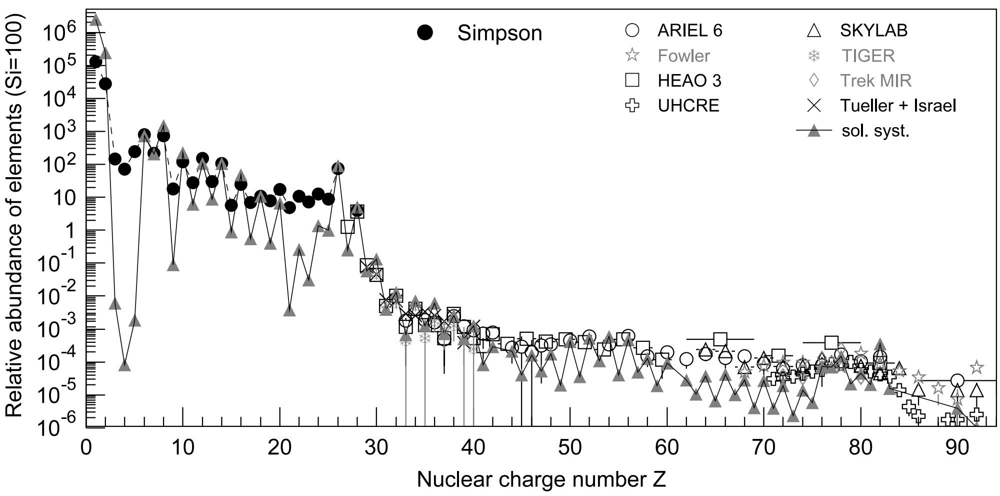

Fig. 2.2.: Mass composition of cosmic rays.
The relative abundance of elements within cosmic rays on the y-axis is plotted against the nuclear charge of the element on the x-axis at 1 GeV/nucleon. Both axes are unit-less. The y-axis is logarithmic while the x-axis is linear. The graph is normalized to silicon at a relative abundance of 100. Data from multiple experiments, as listed in the legend and indicated by different data point styles, have been combined. As a reference, the relative abundance of elements in the solar system is shown as well [BEH09].

For higher energy cosmic rays, only indirect measurements of the mass composition are possible adding uncertainties on the mass composition. The early assumption, that UHECR mainly consisted of protons, is not supported by current experimental results as seen in Figure 2.4.

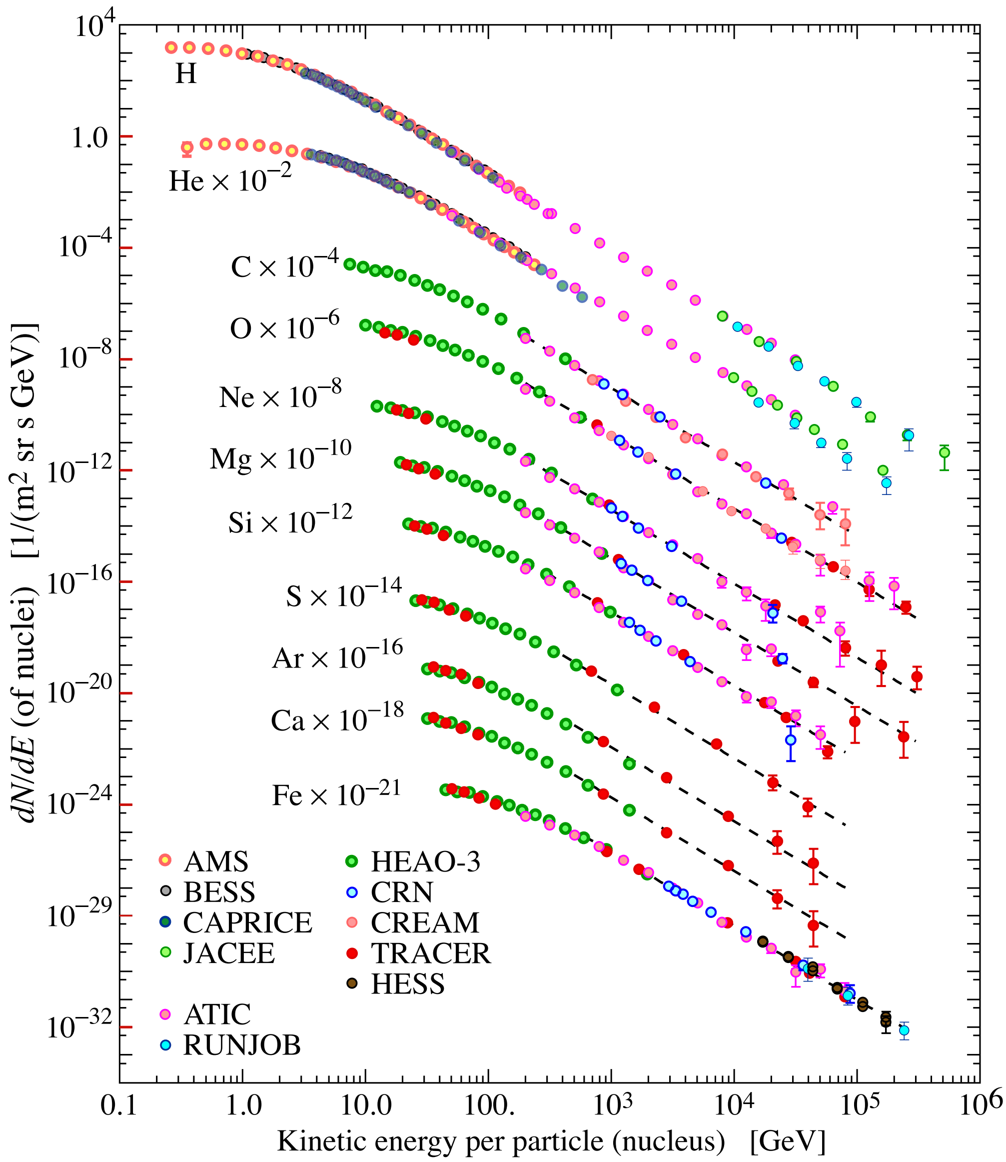

Fig. 2.3.: Flux of cosmic ray particles for different elements and energies. The Figure shows the flux of cosmic ray particles against the cosmic ray particle energy per nucleus grouped for different elements. Both axes are logarithmic. Data from multiple experiments, as listed in the legend and indicated by different data point styles, have been combined [Oli+14].

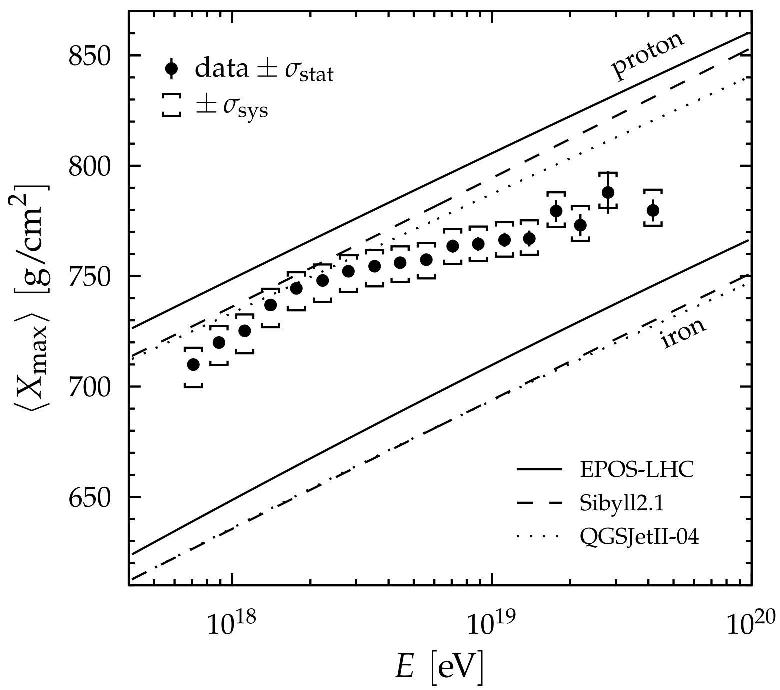

Fig. 2.4.: Comparison between theoretical prediction and measurement of mass composition.
In the Figure, $\langle X_{\text{max}}\rangle$ is plotted against the cosmic ray particle energy per nucleon. $\langle X_{\text{max}}\rangle$ is the integrated atmospheric density from the start of the extended air shower to the point of its maximal particle count. The preliminary measurement of the Pierre Auger Observatory is indicated by black dots. Theoretical predictions for pure iron and proton extended air showers calculated with different interaction models are included. The measured data favors higher mass cosmic particle rays instead of pure proton based cosmic rays for higher energies [Aab+14a].

2.3. Extensive Air Showers

When cosmic rays collide with the atoms of the atmosphere of the Earth, they become the seed of a cascade of particles evolving to the ground. These cascades are called extensive air showers. To distinguish between the cosmic particle and the products of its reaction with the atmosphere, the cosmic particle is called primary while all other particles of the cascade are called secondaries. Depending on the energy and type of the primary particle, different processes can take place within the atmosphere and different secondary particles can be produced. The reaction products of these processes can be grouped into three components, the muonic component, the hadronic component, and the electromagnetic component as delineated in Figure 2.5. Each component evolves differently in the atmosphere and will lead to different particles reaching the ground. Due to accelerator experiments, the interactions between these components and the nuclei of the atmosphere are well known for lower energies but above $E \approx 10^{17}$ eV [Tay08] only the extrapolation of the properties of the interactions is possible.

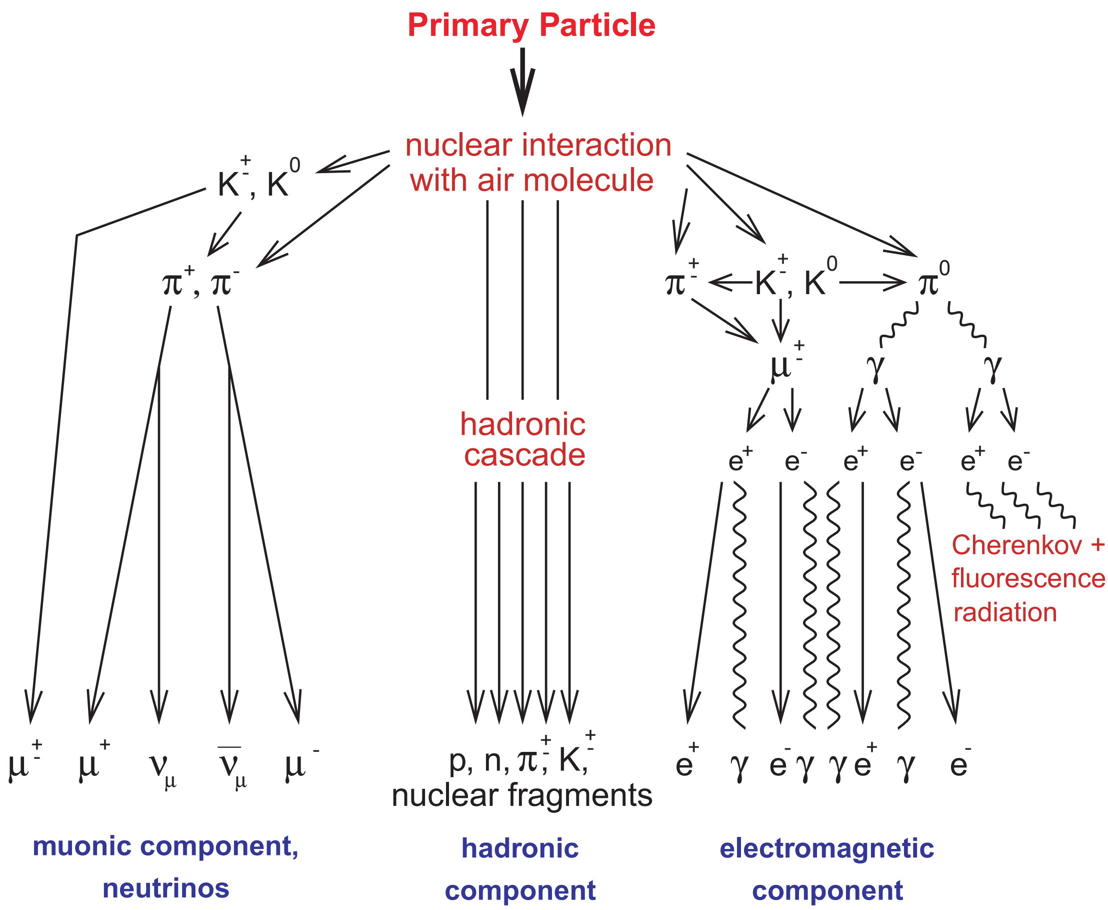

Fig. 2.5.: Schematic air shower.
The three different components of an air shower — electromagnetic, hadronic, and muonic — are shown. The separation of components is only used for illustrative purposes and does not happen in a real extended air shower [RS12].

2.4. Detection

Primary particles can be detected directly utilizing satellite or balloon based experiments. At energies above 10^{14} eV [Spa08] direct measuring methods become unfeasible due to the low particle flux and only indirect measurements based on extensive air showers are viable. Besides the direct detection of secondary particles on the ground, the propagation of an extended air shower through the atmosphere can be measured due to emitted Cherenkov and fluorescence light.

2.4.1. Fluorescence light

Secondary particles traversing the atmosphere of the earth excite the atoms of the air. The atoms return to their ground state by emitting a photon in the wavelength range of 300 to 430 nm [Abr+10a]. The number of photons is proportional to the energy loss of the secondary particles. This light is called fluorescence light.

2.4.2. Cherenkov light

The phase velocity of light in a medium differs from the phase velocity of light in vacuum. A charged particle traversing a dielectric medium polarizes it locally. Once the particle has passed the polarized location, the medium returns to an unpolarized state and in turn, an electromagnetic wave is emitted. While the speed of the particles is below the local speed of light, destructive interference between multiple of the aforementioned waves takes place and no macroscopic wave is formed. If the speed of the particles reaches the local phase speed of light or exceeds it, the electromagnetic waves start to add up to a macroscopic wave which can be seen as light radiating in an angle θ from the particle trajectory as seen in Figure 2.6. This is called the Cherenkov effect [Che34; Che37].

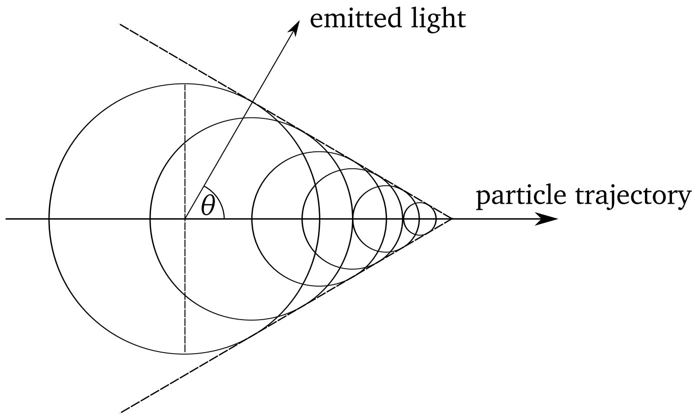

Fig. 2.6.: Cherenkov light in relation to the particle trajectory.
The angle θ between the trajectory of the particle and the emitted light can be seen as well as the electromagnetic waves emitted by the unpolarizing locations of the medium [Czi].

The angle θ is defined by

$$\cos\theta = \frac{1}{n\beta} + \frac{p_{\text{pho}}}{2p_{\text{par}}}\left(1 - \frac{1}{n^2(\lambda)}\right) \tag{2.2}$$

with

n as the refractive index of the medium for a specific wavelength λ,

β as the ratio of the speed of the particle to the absolute speed of light,

p_{pho} as the momentum of the photon, and

p_{par} as the momentum of the particle [Gin40].

The term $\frac{p_{\text{pho}}}{2p_{\text{par}}}\left(1 - \frac{1}{n^2(\lambda)}\right)$ can be ignored for most media as the momentum of the photon is negligible. The angle θ does not depend on the rest mass of the particle but only on its velocity.
The second characteristic variable is the number of emitted photons in a defined wavelength range per distance traversed by the particle

$$\frac{dN}{dx} \propto \int_{\lambda_1}^{\lambda_2} \left(1 - \frac{1}{n^2(\lambda) \times \beta^2}\right) \frac{d\lambda}{\lambda^2} \tag{2.3}$$

where λ_1 to λ_2 is the wavelength range and is also independent from the rest mass of the particle. It only depends on the velocity of the particle [TF37].

3 Pierre Auger Observatory

The Pierre Auger Observatory is a detector array used for the observation of extended air showers. It features a hybrid detector design, composed of two independent detector setups, the Fluorescence Detector (FD) and the Surface Detector Array (SD). The Pierre Auger Observatory is situated in the Pampa Amarilla in Argentina. Extended air showers detected by both the FD and the SD are called hybrid events. Hybrid events can either be used to cross-calibrate the detector systems or to obtain a bigger set of properties for the same extended air shower.

3.1. Fluorescence Detector

The FD is composed of four installations with six fluorescence telescopes each. A schematic view of a single telescope with its components is depicted in Figure 3.1. The four installations are situated around the SD area. Every camera has a field of view of 30°, both azimuthal and polar. The polar field of view starts at ground level. The location of the installations as well as their azimuthal fields of view are shown in Figure 3.2. Secondary particles, traversing the atmosphere of the earths, can excite nitrogen atoms which will emit fluorescence light as seen in Figure 2.5. This light can be detected by utilizing the FD.

The FD is designed to reach the maximal extended air shower detection rate at a primary particle energy of 10^{19} eV. The duty cycle of the FD is limited to about 13 % due to over-illumination by light sources like the sun and the moon [Abr+10a]. The High Elevation Auger Telescopes (HEAT) upgrade has added a fifth installation. The HEAT installation features a construction similar to the other four FD installations but comprises only three telescopes which can be tilted vertically by about 30°. By surveying the high atmosphere, the energy sensitivity of the FD has been extended down to primary particle energies of 10^{17} eV in the part of the atmosphere observed by the HEAT installation [KLA07].

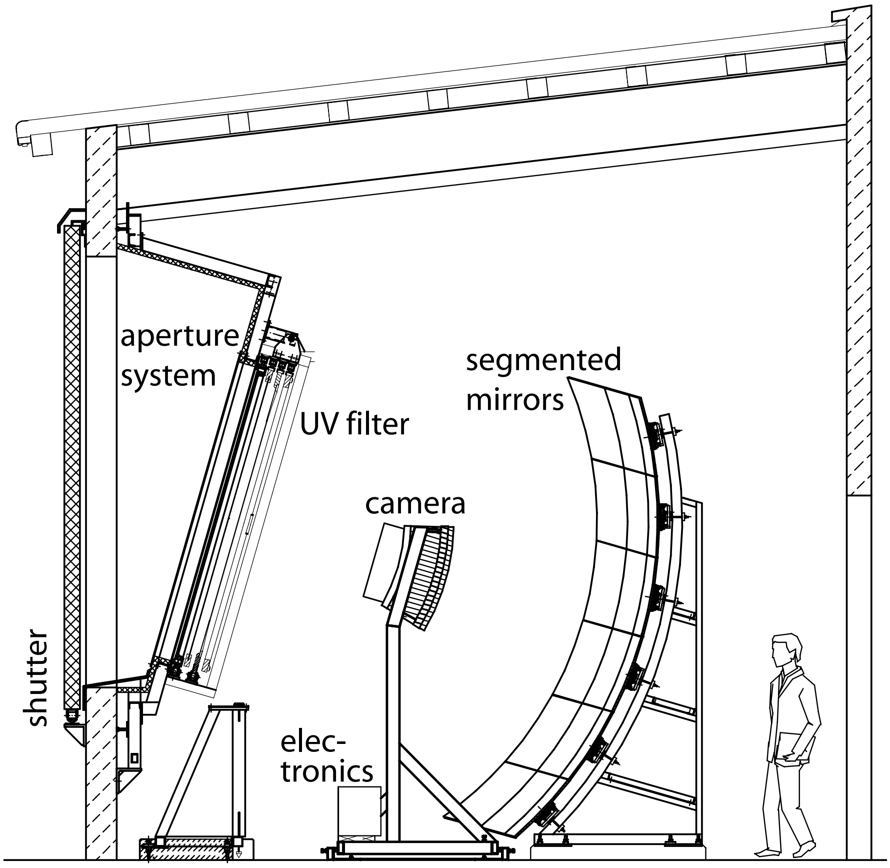

Fig. 3.1.: Schematic view of a single fluorescence telescope.
A schematic view of a fluorescence telescope and its components is shown. Light can pass through the shutter, the aperture system and the UV filter. A segmented mirror is used to focus the light on the camera system. For a size comparison, the shape of a human is included. [Abr+10a]

3.2. Surface Detector Array

The SD consists of more than 1660 individual water Cherenkov Surface Detector Stations (SDSs). The SDSs are placed on a triangular grid with a spacing of 1.5 km covering about 3000 km^2 of ground. Figure 3.2 indicates the position of each SDS in the Pampa Amarilla with a black dot. Refer to subsection 3.2.1 for a description of the internal structure of an SDS. Every SDS works independently and is connected to the Central Data Acquisition System (CDAS) of the Pierre Auger Observatory via a radio link.
The lateral particle distribution of an extended air shower on the ground decreases with decreasing energy of the primary particle. Due to this, the SDS spacing limits the extended

air shower detection rate for lower cosmic particle energies and the maximal detection rate is only reached for a cosmic particle energy of $10^{18.5}$ eV [All+05].

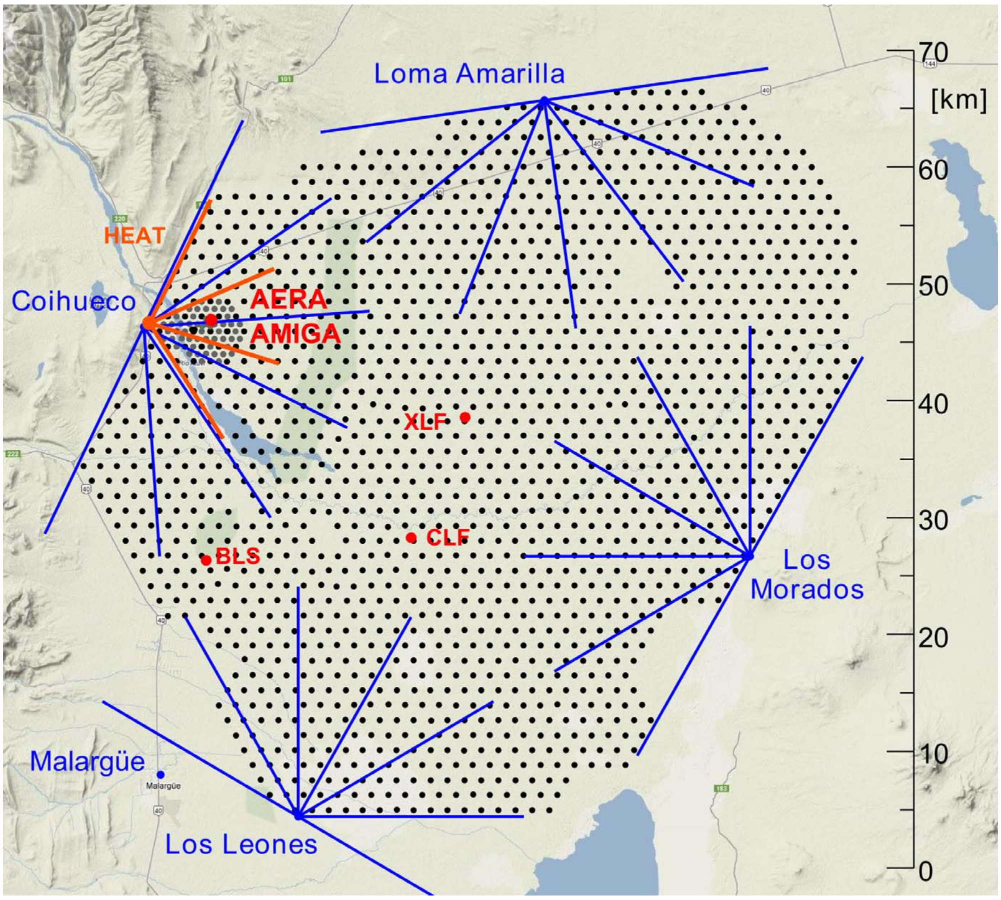

Fig. 3.2.: Map of the Pierre Auger Observatory.
A map of the Pampa Amarilla with the components of both detectors, the FD and the SD. Every SDS is marked by a black dot. All four FD installations are shown. The fields of view of all telescopes are framed with blue (dark) lines. The position of the HEAT installation is shown and its field of view is illustrated in red (light). The map is oriented to the north [Aab+14b].

3.2.1. Surface Detector Station

An SDS is a self-supporting water Cherenkov detector. For a more detailed description of a water Cherenkov detector, see subsection 3.2.3. A picture of an SDS can be seen in Figure 3.3.
Each SDS contains 12000 liters of highly purified water. The water is encased in a approximately circular plastic tank capable to withstand the environmental hazards of the Pampa Amarilla. The tank is approximately circular with a diameter of about 3.6 m and a height of about 1.6 m. Three photomultiplier tubes (PMTs) are optically connected to the water. They are used to detect Cherenkov radiation emitted by relativistic, charged particles passing trough the water. The PMTs are plugged into high voltage generating PMT bases [Gen+01], which are controlled and monitored by the Unified Board (UB). Each PMT has two signal lines, the anode and the dynode line, which represent different amplification levels of the signal. The signal lines are connected to the Front-End card. The Front-End card contains multiple analog digital converters (ADCs) and a field programmable gate array (FPGA) to process the signal in real time. The ADCs have a 40 MHz sampling rate and a 10 bit dynamic range. The Front-End card is plugged onto the UB.
All components of the SDS are connected via a single electric interconnection board, the UB. The UB is a custom made printed circuit board (PCB) and includes a PowerPC (PPC). Time synchronization is supplied by a commercial global positioning system (GPS) receiver plugged onto the UB. For data transmission, the UB is connected to a custom radio, the Subscriber Unit (SU). All communication with the CDAS is conducted utilizing the SU. The SU uses the industrial, scientific and medical (ISM) radio band and allows for up to 1200 bits per second to be transmitted [Abr+10b]. The operating system installed is a Unix derivative. Figure 3.4 shows a picture of an UB with the connections necessary for a basic test.
The complete SDS is solar powered and includes a battery buffer for data taking during the night to achieve a 24 hour duty cycle. Over voltage protection and power distribution is achieved by the UB [All+08].

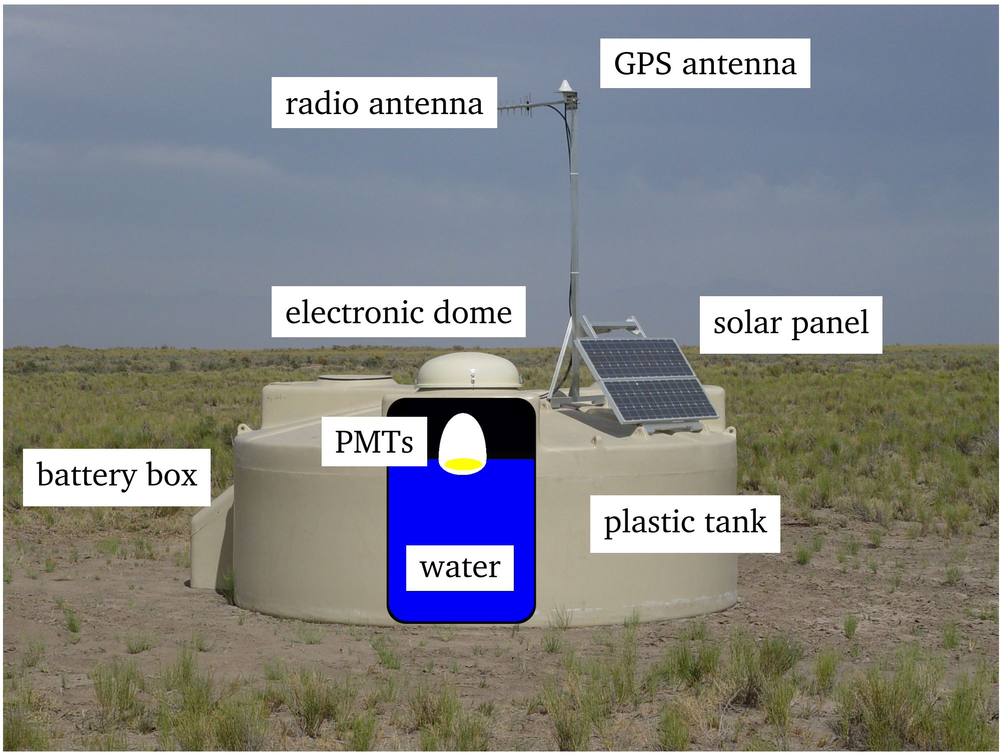

Fig. 3.3.: Picture of SDS #358.
A picture of the SDS #358 with a schematic sectional drawing of a PMT and the embedded water is shown. The UB is installed below the electronic dome. The antennas, the battery box, and the solar panel can be seen. Text labels were added to indicate the position of the components [Pro15].

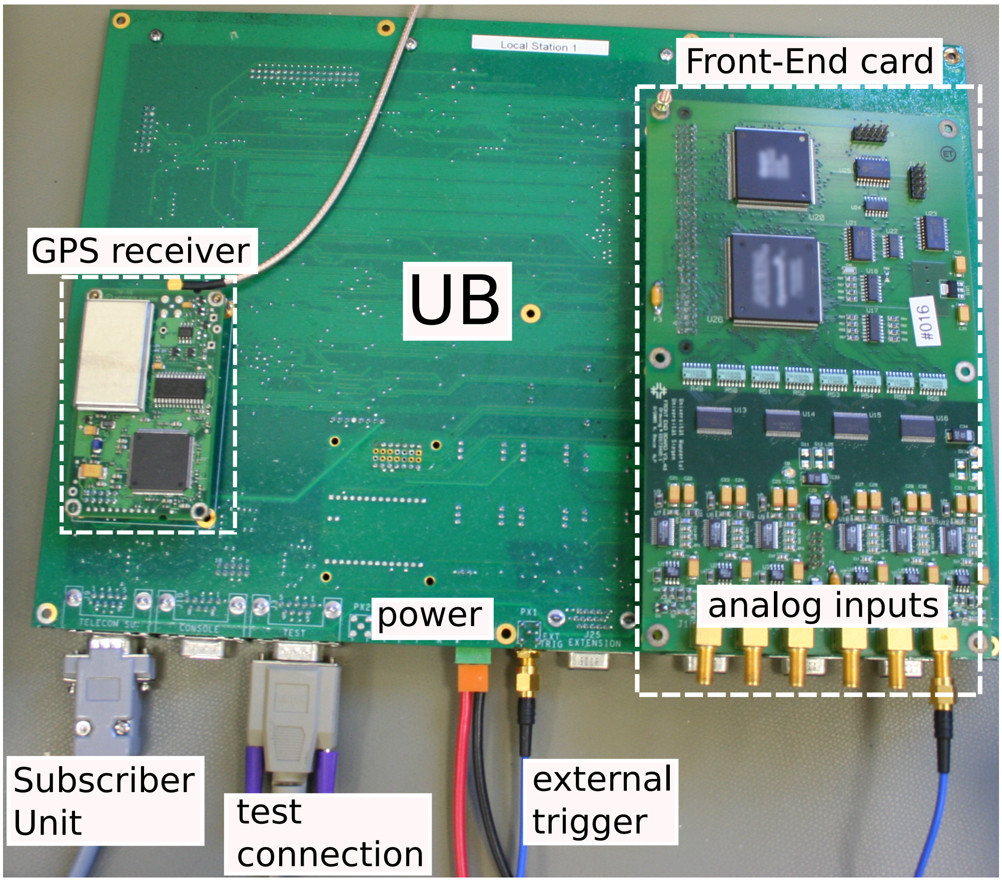

Fig. 3.4.: Picture of an UB.

A picture of an UB is shown. The GPS receiver and the Front-End card are plugged onto the board. The connections to the SU and the power connector can be seen. One of the six analog inputs is connected to an analog signal source for testing purposes. Additionally, a external trigger line and a serial test connection are connected.

3.2.2. Trigger system

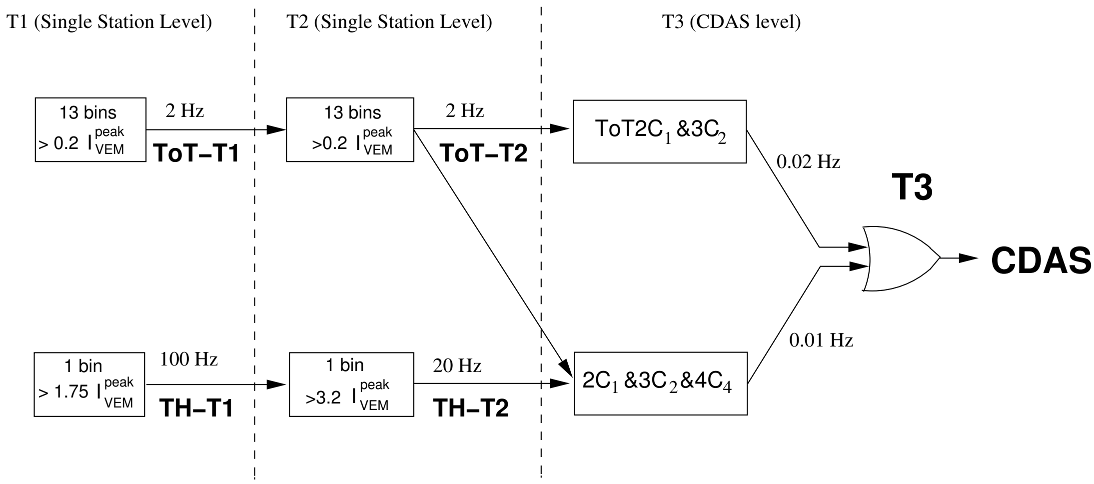

Fig. 3.5.: Hierarchical trigger system of the SD.
The different trigger levels of the SD and their propagation are shown. In this Figure, $I_{\mathrm{VEM}}^{\mathrm{peak}}$ refers to the average peak pulse height recorded by the PMTs for a vertical and centrally traversing muon and bin refers to one sampling point. The trigger rate for each level is given. In this Figure, C_n refers to different types of coincidence between SDSs in the SD [Abr+10b].

The SD features a hierarchical trigger system as seen in Figure 3.5. The first two stages of the trigger system, the T1 and T2 trigger levels, are single station based triggers and are applied inside every SDS. As every PMT installed inside the SDS does have different amplification characteristics, the T1 and T2 triggers are defined in respect to the average peak pulse height recorded by each PMT for a vertical and centrally traversing muon called $I_{\mathrm{VEM}}^{\mathrm{peak}}$. $I_{\mathrm{VEM}}^{\mathrm{peak}}$ is automatically updated every 60 s.
Two independent modes are used to generate trigger signals. The first mode is a Threshold (TH) trigger. If the signals recorded by all the PMTs of a SDS exceed $1.75 \times I_{\mathrm{VEM}}^{\mathrm{peak}}$, a T1-TH trigger is generated, if the signals also exceed $3.2 \times I_{\mathrm{VEM}}^{\mathrm{peak}}$, an T2-TH is generated as well.
The second mode is a Time over Threshold (ToT) trigger. If the signals recorded by at least two out of three PMTs exceed $0.2 \times I_{\mathrm{VEM}}^{\mathrm{peak}}$ for at least 325 ns, both a T1-ToT and a T2-ToT are generated.
The separation between the T1 and T2 is due to bandwidth concerns. While every T1 will be stored with the recorded data for 10 s, only T2 triggers, containing the time stamp and a tank identifier are transmitted to the CDAS. If a coincidence between neighbored SDSs is detected, a T3 is generated and the data acquisition is performed by the CDAS.

3.2.3. Water Cherenkov detectors

In the SDS, a water based Cherenkov detector is used to detect light emitted by traversing relativistic, charged particles, mainly muons and electrons. For a description of the Cherenkov effect, see subsection 2.4.2.
The number of Cherenkov photons emitted by particles passing through water does not depend on the rest mass of the particles. The number of emitted photons per traversed distance $\frac{dN}{dx}$ is the same for an electron and a muon passing the water of the SDS. Yet the two particle types can be distinguished due to their different absorption length in water. While muons travel through the whole tank without being absorbed, the electron will be absorbed after only a few centimeters. Due to this, a single electron will in total emit less Cherenkov light than a single muon.
In the SDS, the emitted Cherenkov light inside the water is detected by utilizing three PMTs. Each PMT can detect single photons, but if photons arrive in rapid succession, the individual signals will pile up to a single signal with a higher amplitude. During a typical extended air shower, multiple electrons pass through the detector while there is rarely more than one muon at a time inside the detector. The result is a signal similar in height but different in shape so the complete pulse form has to be taken into account to distinguish between electrons and muons.

3.3. Planned Upgrades

The analysis of data taken with the Pierre Auger Observatory up to now gave rise to new key science objectives [Col13]:

- The origin of the flux suppression is to be elucidated.
- The mass composition at the highest energies is to be determined.
- The flux contribution of protons up to the highest energies is to be measured.
- Ultra-high energy extensive air showers and hadronic multiparticle production are to be understood.

For the SD, these objectives require upgrades of the composition separation capabilities of each SDS, namely the electron muon separation. To obtain a better muon electron separation, it was recommended to implement an upgrade called Surface Scintillator Detector (SSD), formerly known as Auger Scintillators for Composition II (ASCII), and install a new version of the UB, called the Upgraded Unified Board (UUB) in all SDSs [Ber+14]. SSD will add a scintillator on top of the SDS, which will require two PMT input channels on the UUB.

3.3.1. Upgraded Unified Board

The UUB will be a drop-in replacement for the UB. Consequently, it will fulfill the same role as a central electric interconnection and have compatible connections to the auxiliary systems. Internally, it will feature ten ADC channels where the UB had six ADC channels, both internal and external. Externally, seven analog inputs can be connected to the UUB as three analog input channels will be sampled at two different amplifications. The sampling rate of the ADC channels will be increased from 40 MHz to 120 MHz and the dynamic range will be twelve bit instead of ten bit. The Front-End card will not be reused and its functionality will be integrated into the PCB of the UUB.
The timing resolution of the UUB will be improved due to a new GPS receiver.
The UUB will include a light generator unit for PMT testing and a monitor system by Slow Control (SC). The SC will control all internal power supplies of the UUB and perform a Failure Detection, Isolation, and Recovery (FDIR) process on them. All sensors previously monitored by the UB will be managed by the SC. An additional water temperature sensor and an atmospheric pressure sensor will be added. The SC will provide an ethernet connector and multiple universal serial bus (USB) connectors for debugging purposes [Sta14; Sta15].
A test system for the UUB is in development. How to test the seven analog inputs of the UUB will be presented in the next chapter.

4 Tank Simulator Analog Output

The Tank Simulator (TS) is a modular test system for the digital and analog part of the Upgraded Unified Board (UUB). It is currently under development by the astroparticle physics group of the Siegen University. The TS will generate all signals which are needed to fully emulate all systems of a Surface Detector Station (SDS) necessary to test the full functionality of the UUB. Power supply, analog inputs, external sensors and an emulation of the Subscriber Unit (SU) will be supplied by the TS [Sta15]. The UUB will have seven analog input channels, sampled at 120 MHz with 12 bit precision. The signals produced by the analog output of the TS need to be usable to test the analog inputs of the UUB. Therefore, the analog outputs of the TS have to fulfill multiple requirements:

- The amplitude of the signal has to be adjustable between 0 and -2 V with a yet to be determined dynamic range.
- The timescale and shape of the signal must be similar to the timescale and shape of a photomultiplier tube (PMT) signal.
- The analog output must be able to supply multiple signals with a precision defined time offset for coincidence testing.

Two different methods to generate analog pulses for the test of these inputs of the UUB have been considered. This work focuses on the multiplier method.

4.1. Parallel Digital Analog Converter Method

The parallel digital analog converter (DAC) method generates analog pulses by feeding a digital waveform pattern to a parallel DAC. This means that any waveform can be produced within the physical limits of the DAC. To the first order, these limits are due to the limited sampling rate, the limited full range, and the limited dynamic range of the DAC. Full range describes the difference between the minimal and the maximal amplitude producible by the DAC. Dynamic range describes the minimal difference between two amplitudes producible by the DAC. Another disadvantage is the count of high speed data lines needed by the parallel DAC. For each bit needed to describe the waveform at each sample point, at least one data line is needed per channel. Each data line needs to transmit information at least the sampling rate of the parallel DAC. E. g., a parallel DAC with a 500 MHz sampling rate and a dynamic range of 14 bit needs 14 data lines per channel, which transmit data at least 500 MHz. A prototype printed circuit board (PCB) to test this method has been produced.

4.2. Multiplier Method

The multiplier method generates analog pulses by multiplication of a digital pulse with an analog multiplication voltage. The width of the signal is defined by the length of the digital pulse, while the analog multiplication voltage defines the pulse height. This limits the theoretical shape of the waveform to a rectangle. The rectangular signal needs to be shaped into a PMT like signal. With this method, only the amplitude and length of the waveform can be changed. The bandwidth needed is negligible as the DAC is only programmed once per amplitude change. Hence, the PCB design needs to feature only one high speed line per channel and the design becomes easier in comparison to the DAC method.

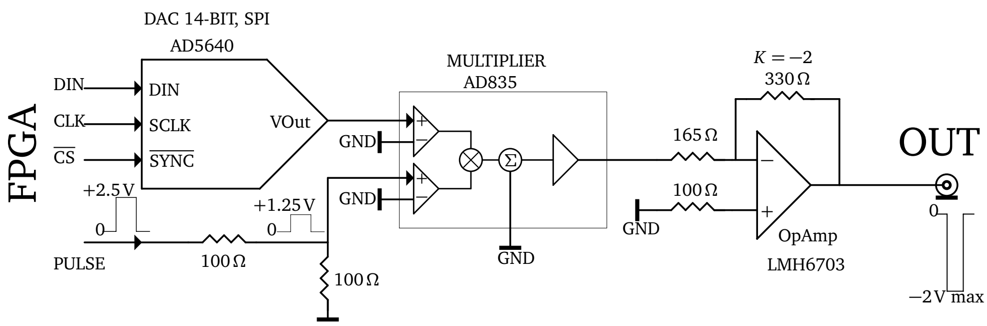

Fig. 4.1.: A single channel of the multiplier card.
One of the eight channels of the multiplier card prototype is shown. The FPGA is connected to the lines on the left hand side. The DAC is programmed via an SPI and connects to one differential, positive polarity input of the multiplier. The second differential, positive polarity input of the multiplier is connected to the FPGA with a voltage divider in between. Both negative polarity inputs of the multiplier are connected to ground. The signal of the multiplier is passed through an operation amplifier with a constant amplification factor of −2.

4.2.1. Multiplier Card Prototype

To determine, if the multiplier method is a viable way to generate analog signals to test the UUB, a prototype card was designed and produced [KV14]. The initial commissioning, software creation and testing was accomplished. The digital pulse is generated by an field programmable gate array (FPGA) and the analog multiplication factor is set by a DAC. A picture of the prototype card can be seen in Figure 5.3. The prototype card connects to the FPGA via a single width, low pin count FPGA Mezzanine Card (FMC) [Bak+10] connector on the input side. On the output side, it features eight analog signal channels. The card is powered with +6 V and −6 V by an external power supply. A single channel of the card can be seen in Figure 4.1. Every channel has four connections to the FMC,

- data in (DIN),
- clock (CLK),
- inverted chip select ($\overline{\text{CS}}$), and
- FPGA pulse (PULSE).

The PULSE line is directly connected to one input of the multiplier chip. DIN, CLK, and $\overline{\text{CS}}$ are connected to the DAC. The output of the DAC is connected to the other input of the multiplier chip. Following the multiplier chip, the signal is amplified by a constant, inverting factor of $K = -2$ using an operational amplifier. The resulting signal is called the output signal of the channel.
The DAC is programmed via an serial peripheral interface (SPI), consisting of DIN, CLK, and $\overline{\text{CS}}$. An SPI is a synchronous serial port. Data is transmitted digitally as seen in Figure 4.3. Once $\overline{\text{CS}}$ is set to logical 0, the logical value on DIN is read with every falling edge of CLK. The specification of the DAC defines a voltage level above 2 V as a logical 1 and a voltage level below 0.8 V as a logical 0. Hence, the digital output pins of the FPGA are operated in the low voltage complementary metal oxide semiconductor (LVCMOS) [JED07] mode at a logic level of 2.5 V. The DAC has a dynamic range of 14 bits and reads 16 bits before setting the output voltage [Deva]. It is programmed at a clock speed of 10 MHz. Setting the DAC value and, therefore, the multiplication factor takes 1.6 µs. While DIN and CLK could be shared between all SPIs, this was not done for the prototype because the FMC connector offers enough data lines. Sharing the DIN would save one digital output pin of the FPGA per DAC but would limit the ability to program all DACs at the same time. Sharing the CLK would also save one pin but would require an additional clock distribution system on the prototype card.
Due to the FMC connector specifications, the SPI lines and the PULSE line have the same

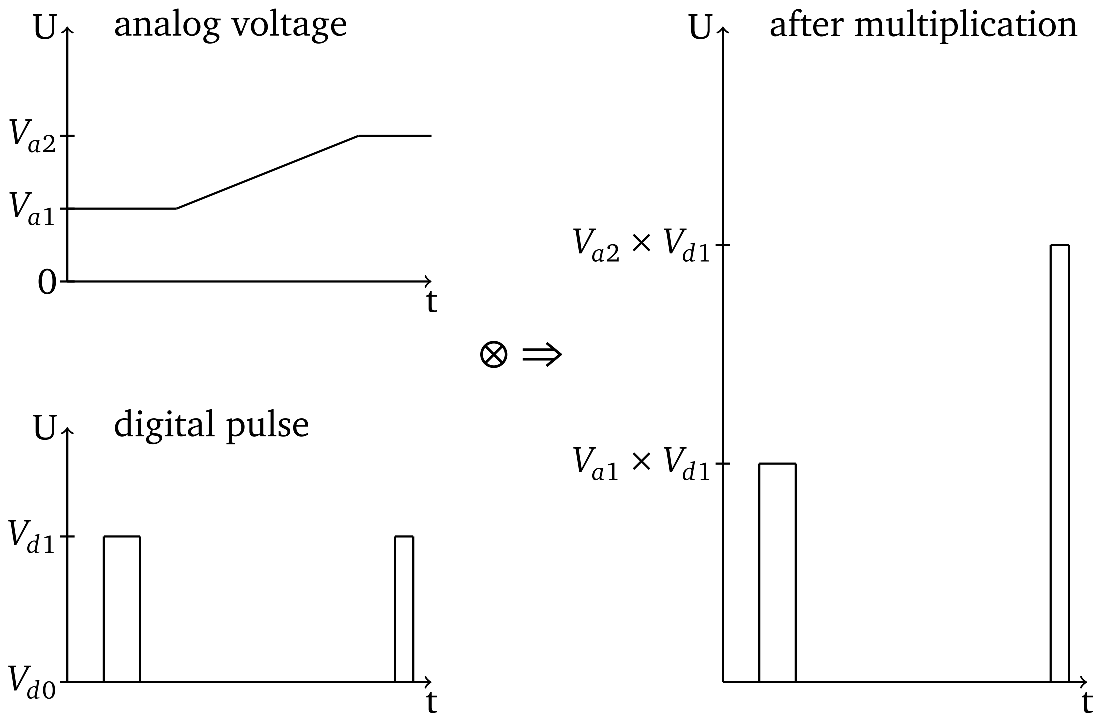

Fig. 4.2.: Schematic view of the idea of the Multiplier Method.
A schematic view of the idea of the Multiplier Method is shown. The upper, left diagram shows the slow changing, analog multiplication voltage. The lower, left diagram shows the fast, digital pulses with fixed amplitude but variable length. The right hand side diagram shows the multiplication of the analog voltage and the fast, digital pulse. On all diagrams, the x-axes represent time, the y-axes represent voltage levels. V_{d1} and V_{d0} are the voltage levels of a logical 1 and 0. V_{a2} and V_{a1} are two examples of possible analog voltages.

voltage level. As the multiplier is linear only for input voltages up to 1 V [Devb], a voltage divider is used on the prototype card to lower the signal on the PULSE line down to 1.25 V. This voltage divider will not be needed for future designs of the card as a different connector will be used. The FPGA used can produce digital signals at a rate of up to 800 MHz, hence the theoretical minimal digital pulse length is 1.25 ns. The maximum digital pulse length is not limited.
In summary, the prototype card can produce pulses with an amplitude from 0 V to −2 V and with lengths as multiples of 1.25 ns.
The FPGA [Xil15] is installed on an evaluation card with multiple external connections. For this setup, only the FMC connectors, a universal serial bus (USB) connection to program the FPGA, and one button to define a reset signal are of interest.

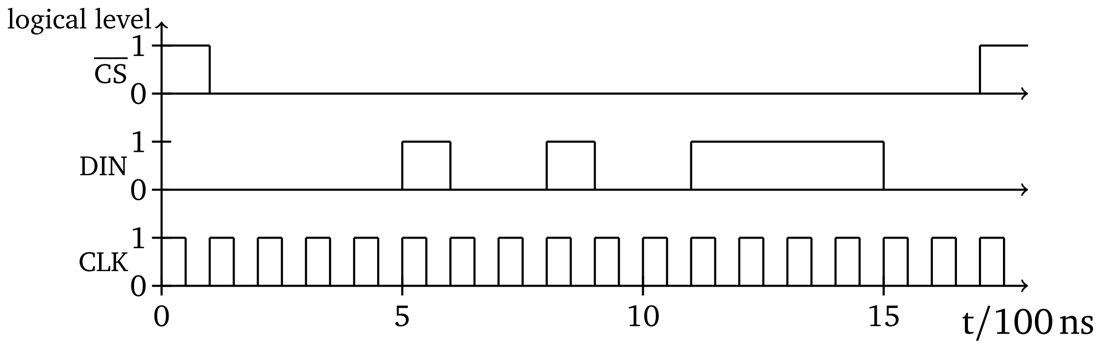

Fig. 4.3.: Recorded signals of the SPI
An example of the recorded signals on the three SPI lines for one channel is shown. The signals were recorded using a logic analyzer. The y-axis shows the logical states of the lines. The x-axis shows the time in units of 100 ns (1/10 MHz). The transmitted value is 0000100100111100 in base 2 or 2364 in base 10.

4.2.2. Software

For each test of the prototype card, special FPGA firmware has been written. One channel of the prototype card was tested at a time. The kind of test is determined by the FPGA firmware. The FPGA firmware was written in the Very High Speed Integrated Circuit Hardware Description Language (VHDL).
To make code reusable, the code was split into three main parts, a finite state machine as a command unit, a standard SPI handler to set the amplitude of the DAC to a digital DAC value (DDV), and an abstraction class, which generates all output signals transmitted via the PULSE line. This split can be seen in Figure 4.5. All firmware uses one button of the evaluation card to generate a reset signal and a synchronization to an external signal. The reset signal will force the state machine into a predefined state to ensure proper operation after the FPGA was programmed with the configuration.
The abstraction class inherits three parameters from the commanding unit to produce a symmetric pulse train. The pulse train model was chosen as it allows for single pulse tests on one channel and coincidence tests between multiple channels. A schematic view of a pulse train can be seen in Figure 4.4. In this context, symmetric means that every pulse of the pulse train has the same length and amplitude. The time between pulses is always the same as the length of the pulse itself. Different parameters can be used for different channels at the same time leading to different pulse trains being produced on different channels. They are still linked to the same temporal point of reference.

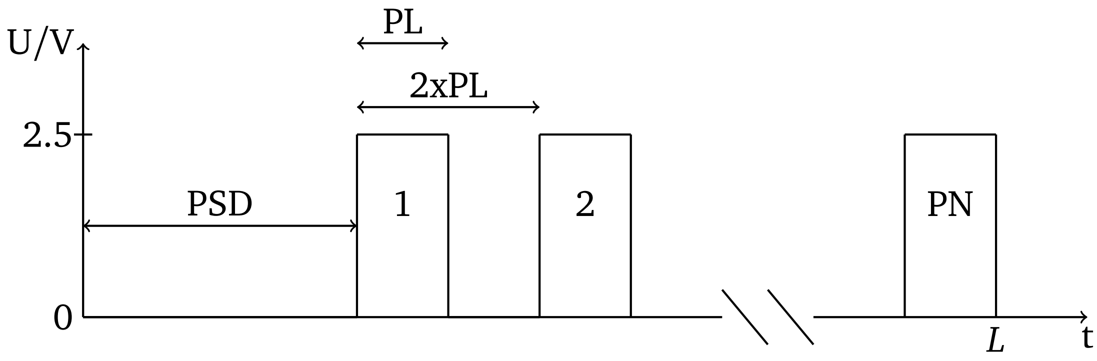

Fig. 4.4.: Schematic view of a pulse train as produced by the FPGA
A schematic view of a digital pulse train as produced on one output channel of the FPGA is shown. The time is shown on the x-axis and the signal amplitude is shown on the y-axis. As digital pulses are shown, the amplitudes of the pulses are always the same. The $t = 0$ position is a point of reference, common to all channels. L marks the end of the pulse train as calculated by Equation 4.1. All three parameters, PSD, PL, and PN are indicated. The PSD defines the relative shift of the first pulse of the pulse train to the $t = 0$ position. The PL defines the length of one single pulse of the pulse train. The PN is the count of pulses in the pulse train.

The parameters are

- the pulse start delay (PSD),
- the pulse length (PL), and
- the pulse number (PN).

The unit of PSD and PL is *output clock cycles*. While the abstraction class can use any clock as a point of reference for the definition of *output clock cycles*, all FPGA configurations use the same 800 MHz clock. Hence, one *output clock cycle* is equal to 1.25 ns (1/800 MHz). The PSD can be used to have defined phase differences between pulse trains on multiple channels. The PL is the length of a single pulse in the pulse train. The PN is unit-less and is the number of pulses in the pulse train. Therefore, the complete pulse train has a length of

$$L = (\text{ PSD} + \text{ PN}(2 \times \text{ PL} - 1)) \times 1.25\,\text{ns}. \tag{4.1}$$

These parameters are used by the abstraction class to generate the pulse train.

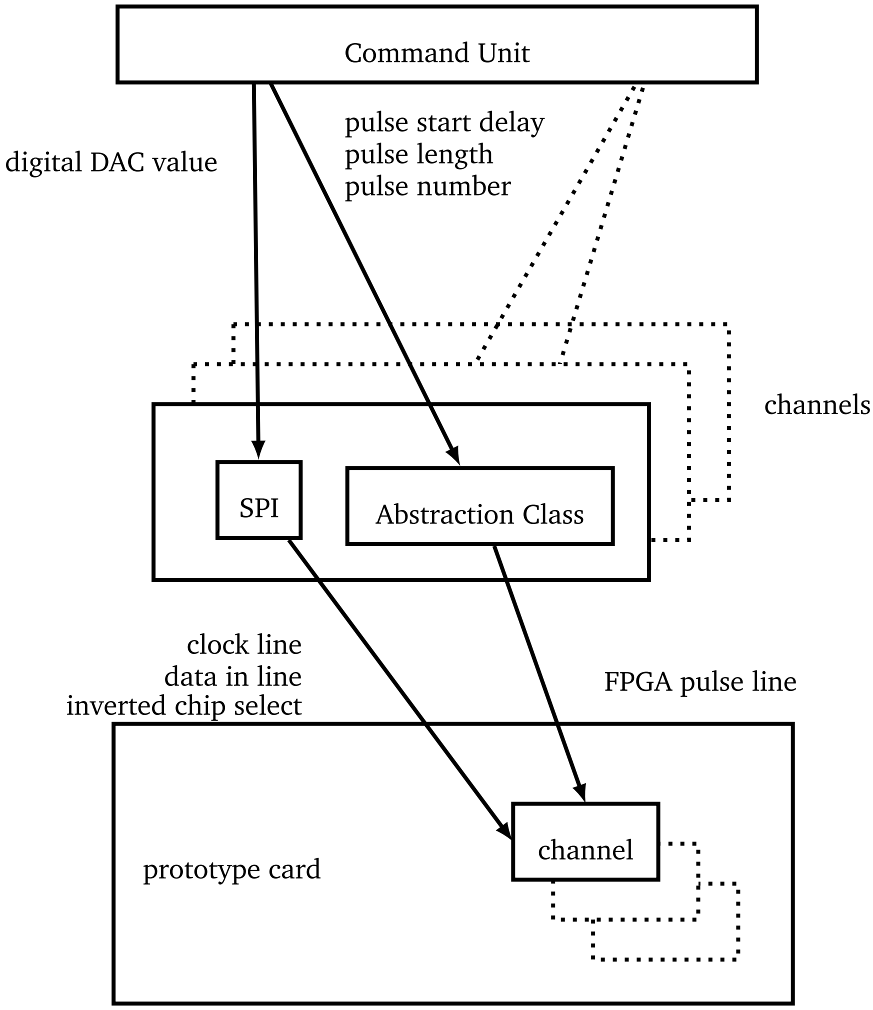

Fig. 4.5.: Schematic view of the VHDL blocks for one channel.
A schematic view of the structures inside the VHDL code can be seen. The command unit defines the parameters used by the SPI block and abstraction class block. The SPI block handles the complete transmission of the DDV. The abstraction class generates the pulse train. Both the SPI and abstraction class block only handle one channel while the command unit block is connected to all blocks of all channels.

Different pulse trains can be produced simultaneously on all eight channels. All channels use the same internal clock and are synchronized to the same point of reference, the $t = 0$ position in Figure 4.4. The DDV is given as a digital unit-less value and defines the multiplication factor

$$\mathrm{DDV} \times \frac{2.5\,\mathrm{V}}{2^{14}} \approx \mathrm{DDV} \times 0.15\,\mathrm{mV} \tag{4.2}$$

at the multiplier. While the DAC can produce voltages of up to 2.5 V, the multiplier is linear only for input voltages below 1 V [Devb]. Therefore, the voltage of the DAC needs to be limited. Due to this, the DDV was limited to $\frac{1\,\mathrm{V} \times 2^{14}}{2.5\,\mathrm{V}} \approx 6666$. This would translate to a dynamic range of $\log_2(6666) \approx 12.7$ bits. As the UUB has a dynamic range of 12 bits, the dynamic range of the prototype card is $\frac{6666}{2^{12}} \approx 1.6$ times the dynamic range of the UUB. While DDV is proportional to the multiplication factor, the multiplier reacts different to short and long pulses for the same multiplication factor. Due to this, a calibration is needed to establish a link between DDV and the peak amplitude of the pulse.

The propagation of the parameters is predefined by the FPGA configuration. E. g., there is an FPGA configuration which increments PL with every external synchronization pulse so the first pulse train only contains 1.25 ns wide pulses, the second only 2.5 ns wide pulses, and so on, up to a predefined maximum. Once the maximum is reached, PL will be set to the starting value and the cycle repeats.

5 Measurement System

To measure the performance of the prototype card of the multiplier method (PTC), an automated measurement system (AMS) was set up. A schematic view of the AMS can be seen in Figure 5.2. The PTC is connected to a field programmable gate array (FPGA) on the input side and to an oscilloscope on the output side. Power is supplied to the card via a power supply. The room temperature is kept at 24 °C using an air conditioning unit. The FPGA is programmed with specialized FPGA firmware depending on the measurement which is performed. A picture of the PTC, connected to the FPGA and the oscilloscope is shown in Figure 5.3.

5.1. Setup

The AMS uses the PTC in a single conversion mode. The signal sent to the PTC is called the synchronization pulse. For every synchronization pulse, the PTC sends two waveforms on two different channels. The first waveform is used to trigger the oscilloscope. This waveform is a single pulse with a length of 100 ns and with a fixed digital digital analog converter (DAC) value (DDV). The trigger system of the oscilloscope is set to react to the falling edge of a signal on the trigger channel at half the signal height. The channel used to produce this waveform is called the trigger channel. Any channel of the PTC can be used as the trigger channel.
The second waveform is produced by the channel under test, called the signal channel. Figure 5.1 shows the delay between the two signals and the measurement window. The parameters used to produce this waveform are called the waveform input parameters (WIPs). The WIPs cannot be read or set by the AMS, but are derived from the previous WIPs after every synchronization pulse. Both, the initial WIPs and the algorithm to determine the fol-

lowing parameters are embedded in the FPGA firmware. The algorithms used are described in section 6.1.
The time delay between the start of the signal on the trigger channel and the start of the signal on the signal channel is long enough that no part of the trigger signal is within the measurement window.

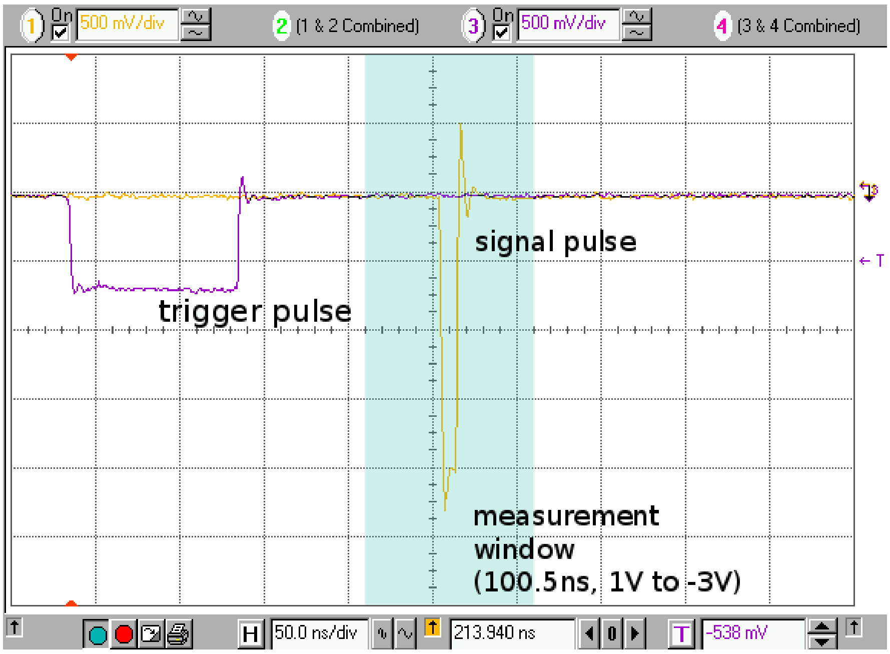

Fig. 5.1.: Oscilloscope picture of the trigger and signal pulses.
An oscilloscope picture of the trigger pulse and the signal pulse is shown. Channel 1 of the oscilloscope is connected to the channel under test of the PTC, channel 3 of the oscilloscope is connected to the trigger signal of the PTC. Labels were added to show which pulse is which. The blue (gray) shadowed region indicates the measurement window during the automated measurements.

All data acquisition is controlled by a software application running on a personal computer (PC), called the data acquisition software (DAS). This PC is connected to a pulse generator, the oscilloscope, which reads out the PTC output, and the FPGA evaluation board to program the FPGA with different FPGA firmware. The pulse generator and the oscilloscope are equipped with a general purpose interface bus (GPIB), which in turn is connected to the PC via a GPIB to universal serial bus (USB) adapter. The pulse generator is used to send the synchronization pulses to the PTC.
For debugging purposes, a logic analyzer can be connected to the second FPGA Mezzanine Card (FMC) [Bak+10] connector of the FPGA via an FMC breakout board.

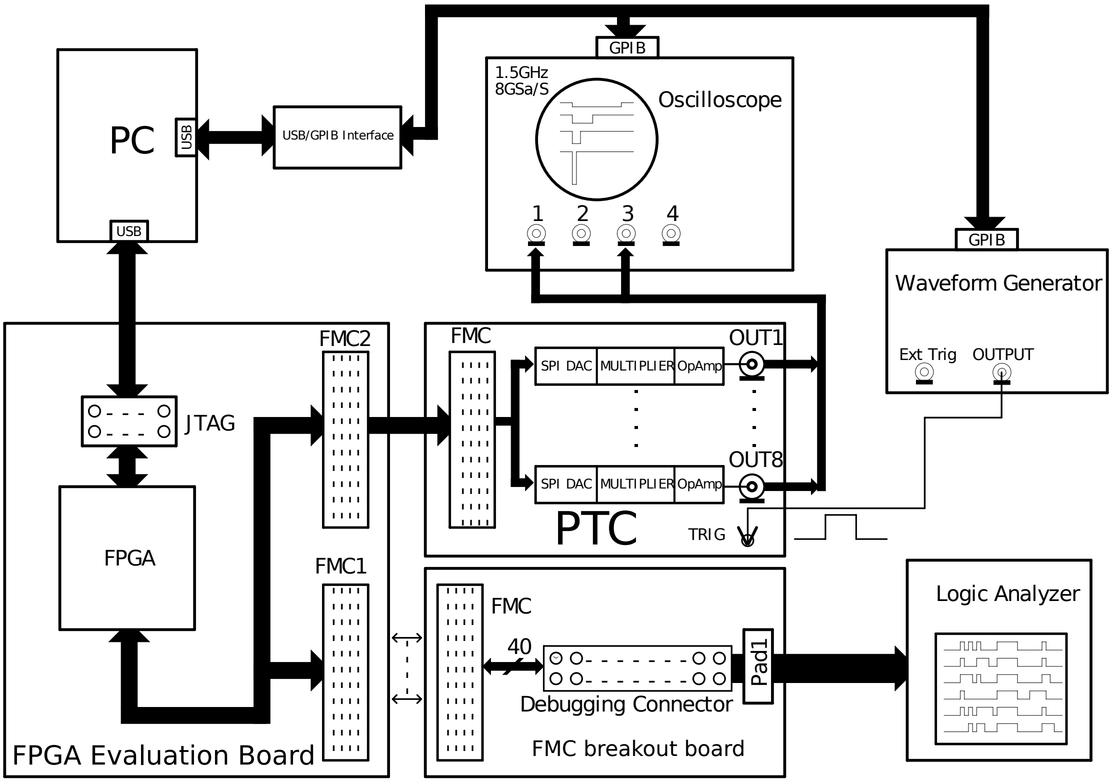

Fig. 5.2.: Schematic view of the AMS for the PTC.

In the upper left corner, the PC is shown. It is connected via USB to the FPGA. Using an USB to GPIB adapter, the PC is connected to the pulse generator and the oscilloscope. The pulse generator is connected to the PTC. The FPGA is connected to the PTC as well as an FMC breakout board. The FMC breakout board is used to connect FPGA pins directly to a logic analyzer. The logic analyzer is used to display debugging information. The debugging information is not included in the automated measurement data. Two outputs of the PTC are connected to the inputs of the oscilloscope. The schematic view is based on [Kol].

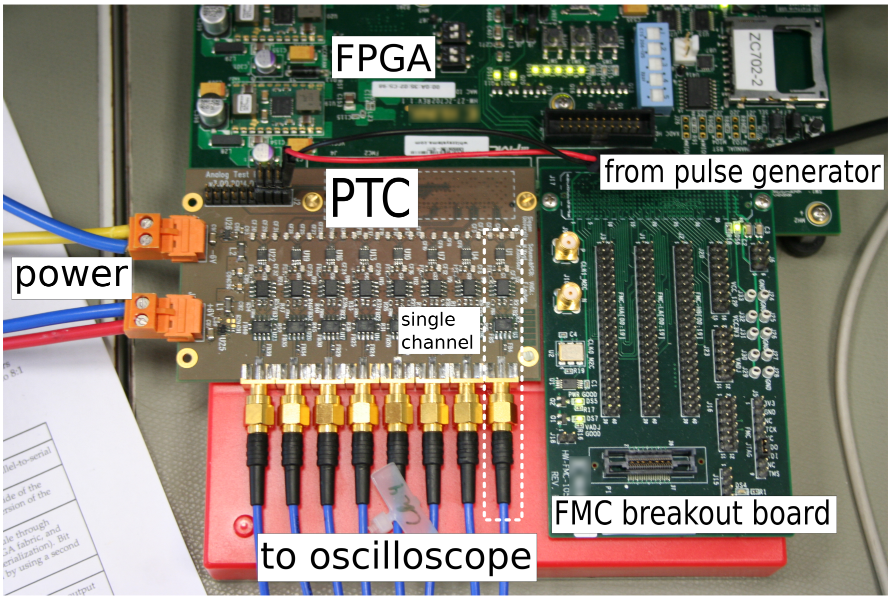

Fig. 5.3.: Picture of the PTC installed in the AMS.
A picture of the PTC, plugged onto the FPGA evaluation board and connected to the pulse generator and oscilloscope is shown. Labels have been added to indicate the different connections and parts of the AMS. The dashed rectangle highlights the first channel of the PTC. Vendor names have been blurred.

5.2. Data acquisition software

The data acquisition software (DAS) automatically reads out the oscilloscope and stores the data for further analysis. The waveforms of one measurement are stored with the WIPs in a streamed tape archiver (TAR) file. Starting from the initial WIPs of the FPGA firmware used for the measurement, the DAS mirrors the algorithm defined in the FPGA firmware. Consequently, the DAS and the FPGA always have the same WIPs.
Once the data acquisition has been started, it repeats the cycle shown in Figure 5.5. Two events interrupt the cycle. The first event is a manual stop of the DAS. If it occurs, no synchronization pulses are sent and no waveforms are produced. The second event is a timeout due to the oscilloscope not registering a trigger pulse within 10 s after the synchronization pulse was sent to the PTC. As the synchronization of the WIPs in the FPGA and the DAS can be lost in such an event, the DAS stops the data acquisition cycle to prevent a wrong association between WIP and recorded waveforms. Already acquired data are not invalidated due to the streaming mode of the TAR file.

5.3. FPGA firmware

Different FPGA firmware exists for different measurements. Each FPGA firmware implements the same logic but differs in the initial WIPs and the algorithm used to calculate the new WIPs after each synchronization pulse.
The implemented logic consists of a set of logical states, the parameter calculation state (pc), the wait state (w), the trigger state (t), and the pulse state (p). One button of the FPGA evaluation board is used as a manual reset signal. If a reset signal is detected, the WIPs are set to the initial value and the FPGA is set to the w state. This signal is needed as the FPGA is in an undefined state after it was programmed.
In the w state, nothing happens until a synchronization pulse is detected. Once this happens, the system transitions into the t state. In the t state, the trigger signal for the oscilloscope is produced and the system moves directly to the p state. In the p state, a signal is produced on the channel under test based on the current WIPs. After the signal has been produced, the pc state takes place. In the pc state, the WIPs for a new waveform are calculated according to the algorithm defined by the FPGA firmware from the current WIPs. After the pc state, the system returns to the w state.
The logical states should not be confused with state machine states as the actual implementation of the logical states is separated into a slow, clocked part for the pc state with a complete state machine for the induction step and a fast, real-time part used to link the w, t, and p states. Due to this, the time between the t and p state is fixed and therefore, the time between the signal on the trigger channel and the start of the signal on the signal channel is fixed as well.

5.4. Oscilloscope

The oscilloscope is programmable via a GPIB interface [Hew02]. Utilizing the GPIB interface, all settings used by the oscilloscope and the stored waveforms can be read out. A summary of all settings necessary to restore the full waveform from the stored waveform data can be requested. This summary is called the preample.
All measurements are performed at a sampling rate of 8 GSa and real time mode. In this mode, the oscilloscope has a bandwidth of 1.5 GHz. Only channel 1 and channel 3 of the oscilloscope can be used in this mode. The full-resolution channel scale was set to 500 mV which translates to a full range of 4 V. The offset was set to -1 V. Therefore, the absolute range of the oscilloscope was 1 V to -3 V. The oscilloscope was set to single shot mode and triggers on a signal on the trigger channel. The spacing between the sample points is defined by the sample rate and is 125 ps.
Per recorded waveform, 804 sample points corresponding to a total time of 100.5 ns are

recorded. A trigger delay was set so that the first 100 sample recorded points (12.5 ns) are taken after the trigger pulse has ended and the signal pulse has not yet started. The analog digital converter (ADC) has an 8 bit resolution and a variable sampling rate with 8 GSa as the maximum. Due to a linearity correction, the actual data taken by the oscilloscope is 16 bit wide as seen in Figure 5.4. The error of the relative voltage between sample points is stated by the manual as 1 % of the full range, which corresponds to ±40 mV.
The error of the offset is ±1 % of the channel offset plus ±1 % of the full scale. Hence, the offset error is ±50 mV. While the average time variation between sample points is stated in the manual as 8 ps, the time error on a measured Δt is stated as $\pm 0.00007 \times \Delta t$ plus an additional 0.2 % of the sampling period Δs [Hew01]. Here, the sampling period was always $\Delta s = 125$ ps and therefore $\sigma_{\Delta t} = \pm 0.00007 \times \Delta t + 25$ ps.

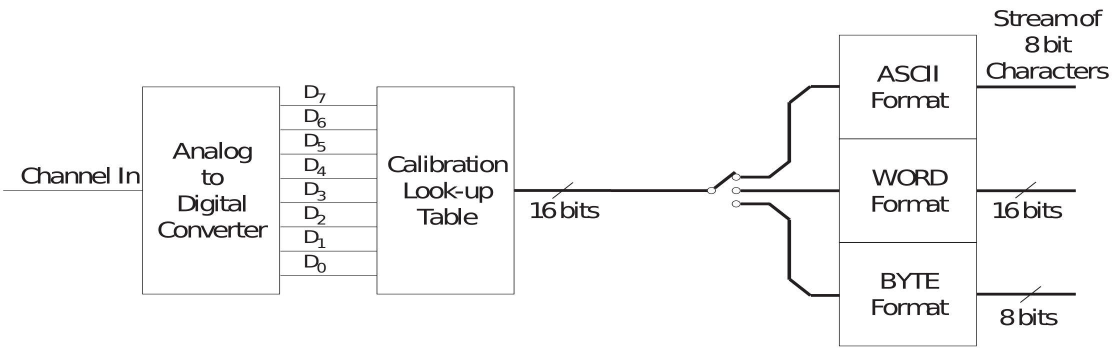

Fig. 5.4.: Schematic view of the data flow inside the oscilloscope.
A schematic view of the data flow inside the oscilloscope for a single channel is presented. The analog output signal of the PTC is attached to the "Channel In" (left) of the ADC. The ADC returns 8 bits which are fed through a "Calibration Look-up Table". The resulting 16 bits can be retrieved in different formats. The formats are the "BYTE format", the "WORD format", and the "ASCII format". For this setup, only the "ASCII format" was used. This means that every sample point is expressed by a floating point number in scientific notation e. g. $-2.34E{-}02$. While the "ASCII format" is the slowest, it also guarantees that the waveform data is stored in a human readable format. The sample points are comma separated. The "Calibration Look-up Table" is obtained during the calibration of the oscilloscope [Hew02].

5.5. Data storage

A measurement is defined as a set of waveforms, which are acquired in succession with the same FPGA firmware and oscilloscope settings.

The signal channel and trigger channel cannot be changed during a measurement. Therefore, a measurement can only contain data from one signal channel and one trigger channel.

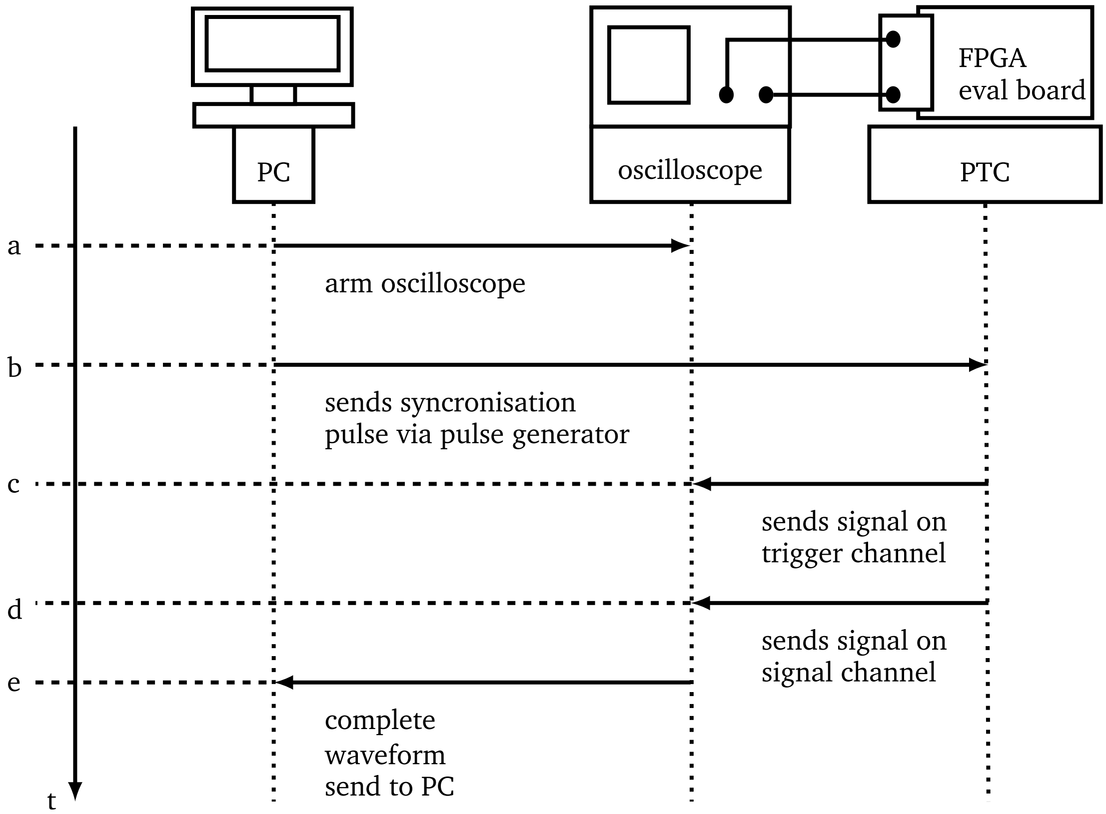

Fig. 5.5.: Interactions between the components of the AMS to acquire a waveform. A schematic with all interactions between the PC, the oscilloscope, and the FPGA with the PTC attached is shown. The chronological sequence is top to bottom. The direction of the horizontal lines indicates the signal flow. In the first step, the PC clears the internal memory of the oscilloscope and arms the trigger system of the oscilloscope (a). Then, the PC sends a synchronization pulse to the FPGA, using the pulse generator (b). The FPGA, after receiving the synchronization pulse, switches from the wait state w to the trigger state t and a trigger pulse is sent to the oscilloscope (c). Once the trigger pulse is sent, the FPGA switches to the pulse state p and the pulse train is sent (d). The time between (c) and (d) is fixed. After this, the new WIPs are calculated (pc) and the FPGA returns automatically to the wait state w. Upon receiving the trigger pulse, the oscilloscope records the output of the signal channel of the PTC. Once the oscilloscope has completed the data acquisition, the PC reads out the recorded waveform (e). After that, the internal memory is cleared and the cycle (a) to (e) repeats.

Each measurement is stored in a single, streamed, flat hierarchy TAR file. In this context, streamed refers to an operation mode where data is only appended to the end of the file without interfering with already written data. Using the streaming mode of the TAR file limits the file to sequential reads but prevents any data loss in an event like e. g., sudden power loss. Flat hierarchy means that all files are stored on the same level (folder) of the file hierarchy.
The first file stored in the TAR file is the preample. The preample is stored as a JavaScript object notation (JSON) [Bra14] string as seen in Appendix B. Every other file is one recorded waveform. The name of the file contains the WIPs (signal channel, trigger channel, pulse number (PN), pulse start delay (PSD), pulse length (PL), and DDV) and a time stamp. The digitized waveform is stored inside the file as an American standard code for information interchange (US-ASCII) [Cer69] string. The values at each sample point are separated by a comma.
To save storage space, the TAR files are compressed during the measurement using the Lempel–Ziv–Markov chain algorithm (LZMA) achieving a reduction of approximately 90 %. Both compressed and uncompressed TAR files are supported by the analysis software.

5.6. Measurement Process

Before every measurement, the FPGA is programmed with the corresponding FPGA firmware. Afterwards, the FPGA has to be set into a defined state by pressing the reset button. This sets the logical state into the wait (w) state and resets the WIPs stored inside the FPGA to the starting values of the current FPGA firmware. The operating cycle of the AMS is shown in Figure 5.5.

6 Analysis

In this chapter, the multi stage analysis of the recorded data is described. The structure of the analysis is outlined in the following enumeration:

1. The selection of the waveform input parameters (WIPs) is discussed

2. The waveforms, which are produced using the prototype card of the multiplier method (PTC) and recorded by the automated measurement system (AMS), are checked for a possible mismatch between the waveform and the recorded WIPs. For each combination of WIPs, a histogram is filled with all waveforms featuring the same WIPs and is visually inspected.

3. A baseline for every waveform is determined and a baseline correction is applied.

4. The waveform is piecewise linearly interpolated.

5. From this interpolated waveform, eight parameters, the waveform characterization parameters (WCPs), are obtained.

6. The WIPs and WCPs are combined and analyzed.

As a convention, $s(i)$ references the i^{th} sample point in the recorded waveform, I references the number of sampled waveforms, and T is the time between two sample points. The implementation of a complete Whittaker-Shannon reconstruction (see section 6.5) was evaluated but within the measurement uncertainties, there are no differences between a Whittaker-Shannon reconstruction and a piecewise linear interpolation. The different reconstructions are described in section 6.5 and section 6.6. In this chapter, if no signal channel is explicitly stated, the signal channel was 1.

6.1. Waveform input parameters

The PTC has to fulfill the following requirements, a more precise description is given in chapter 4:

1. The amplitude of the signal has to be adjustable between 0 and $-2\,\mathrm{V}$, with a yet to be determined resolution.
2. The timescale and shape of the signal must be similar to the timescale and shape of a photomultiplier tube (PMT) signal.
3. The analog output must be able to supply multiple signals with a precisely defined time offset for coincidence testing.

Hence, three relations are determined:

- The behavior of the peak amplitude of the signal as a function of the WIPs (see subsection 6.8.3).
- The behavior of the full width half maximum (FWHM) of the produced signal as a function of the WIPs (see subsection 6.8.4).
- The relative time shift between two signals on two different channels as a function of the WIPs (see subsection 6.8.5).

The WIPs are the pulse start delay (PSD), the pulse length (PL), the pulse number (PN), and the digital DAC (digital analog converter) value (DDV). Since not all parameter value combinations can be tested, the selection of values is described in the following.
As all of these relations are only concerned with single pulse features, the pulse train is reduced to a single pulse by setting $\mathrm{PN} = 1$. The AMS uses one channel of the PTC to trigger the oscilloscope, all measurement windows are temporally aligned within the temporal uncertainty of the AMS and, for a constant PSD, all recorded waveforms are at the same temporal position. Due to this, PSD was set to 0 *output clock cycles*. Hence, only the DDV and PL are altered to measure all relations described above.
The DDV and PL parameter spaces are scanned in the ranges: $1 \leq \mathrm{PL} \leq 15$ and $0 \leq \mathrm{DDV} \leq 6666$. Both DDV and PL are integer values. All combinations of DDV and PL in the given ranges are measured, but the measurement density is not uniform. The DDV value space is to large to uniformly measure all values with high statistics. Hence, eleven equidistant values are chosen for high statistic measurements of the linearity of the pulse height and -width. These DDVs satisfy $\mathrm{DDV} \text{ modulo } 666 = 0$. The PL range is split into 2 regions, the $\mathrm{PL} \leq 5$ region with a high measurement count and the $\mathrm{PL} > 5$ region with a lower measurement count.

All channels have been tested, but only channel 1 was used to record high statistics. In total, 60881399 waveforms have been recorded for channel 1 and 43622630 of these waveforms satisfy DDV modulo 666 = 0. This can be seen in Figure 6.1. For all other channels combined, 4433710 waveforms have been recorded.
For every measurement, an algorithm to calculate the WIPs was chosen to maximize the detection rate of a lost pulse during the measurement. Therefore, any measurement which has a DDV spacing of 1 distinguishes between an odd or even numbered waveform. Two consecutive waveforms use a DDV which is half of the maximal DDV apart. The resulting DDV sequence looks like this: 6667, 3333, 6666, 3332, and so on, down to 3334, 0. If a waveform is lost during the measurement, the sequence of large pulse, small pulse is broken and two large or two small pulses are seen in direct succession. This is detected in the second stage of the analysis by visual inspection. Up to now, no such error was detected.
The PL is increased by one after each completed scan of the DDV range. The PL is changed only after the maximum DDV value was reached. At this point, PL is counted up by one. Once the maximum values of DDV and PL are reached, the DDV and PL are reset and the cycle starts again.

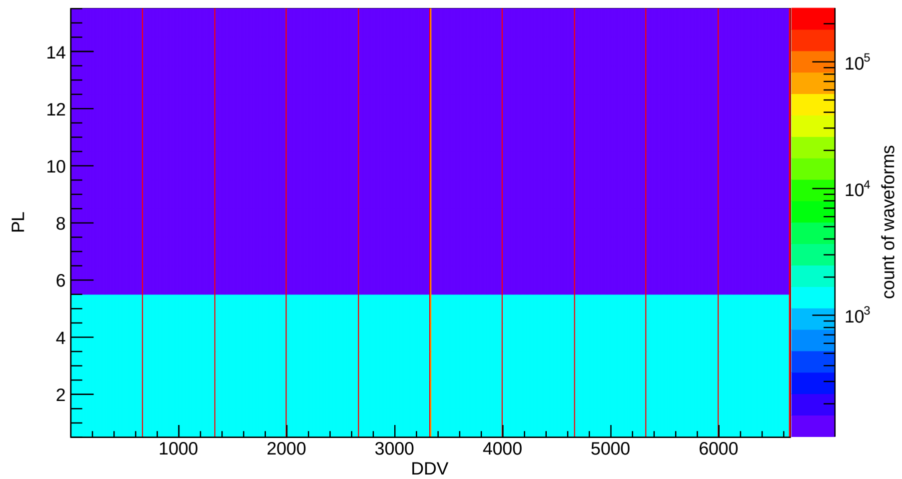

Fig. 6.1.: Number of measured waveforms against the WIPs

A two dimensional histogram is shown. The x-axis shows the DDV, the y-axis shows the PL in *output clock cycles*. The color of each bin indicates the number of measured waveforms for this DDV and PL combination. The x- and y-axis are linear, the color scale is logarithmic. The vertical lines are DDVs, which satisfy DDV modulo $666 = 0$. Beside the vertical lines, no change in measurement density can be seen in x-direction. In the y-direction, the $\text{PL} \leq 5$ region has higher measurement density (order of 10^4) than the $\text{PL} > 5$ region (order of 10^2).

6.2. General waveform discussion

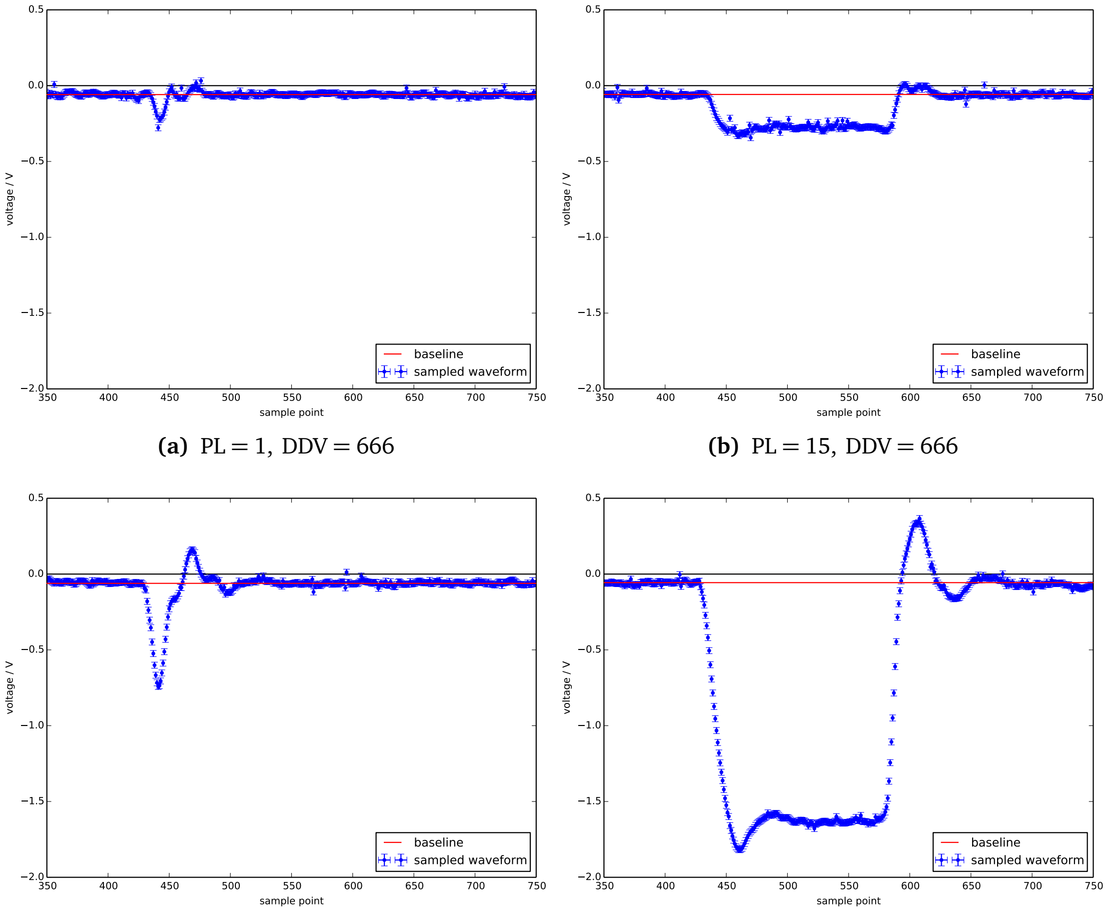

(a) PL = 1, DDV = 666

(b) PL = 15, DDV = 666

(c) PL = 1, DDV = 4662

(d) PL = 15, DDV = 4662

Fig. 6.2.: Four measured waveforms.
Four exemplary, measured waveforms with different combinations of PL and DDV are shown. The DDV and PL values are stated below the plots.

Figure 6.2 shows four exemplary, measured waveforms, each representing a class of a measured waveform. Each waveform is either short (PL = 1) or long (PL = 15) and has either a low (DDV = 666) or a high amplitude (DDV = 4662). While each waveform represents a different class, some characteristics are the same for all waveforms. They all have negative polarity and their baseline is $-60\,\mathrm{mV} \pm 50\,\mathrm{mV}$. A description of the baseline uncertainty is given in section 5.4.
In all recorded waveforms, the main negative pulse is followed by a positive overshoot and a smaller negative undershoot. The amplitudes of these over- and undershoots depend on

the height of the first negative pulse. The reduction of these features by an improved design is not part of this thesis.
The theoretical waveform of all waveforms produced by the PTC is a rectangle as described in section 4.2. For long pulses, this form can be detected as seen in 6.2d and 6.2b. For short pulses, the waveform looks like a single peak instead of a rectangle. For high amplitude, long pulses, there is also a negative undershoot followed by a positive overshoot at the left hand flank of the main pulse as seen in 6.2d. While this overshoot is assumed to be present in all other classes of waveforms, it cannot be detected as the waveform is formed like a peak anyway.
In conclusion, the basic form of the signal is altered by the WIP between a peak like structure and a rectangular like structure. Multiple overshoots can be detected. This will be improved in future versions of the PTC.

6.3. Visual inspection

Before a measurement is evaluated, a visual inspection is performed. All waveforms for one set of WIPs are filled into a two dimensional histogram. An example is shown in Figure 6.3. This figure shows one exemplary histogram, not only for one measurement but for all measurements. As all waveforms share the same WIPs, the waveform like shape in the histogram corresponds directly to these WIPs. Up to now, the visual inspection has not shown any error. If an error would have happened and a waveform had been lost during the measurements, the histogram would contain waveforms with different DDVs and PLs.

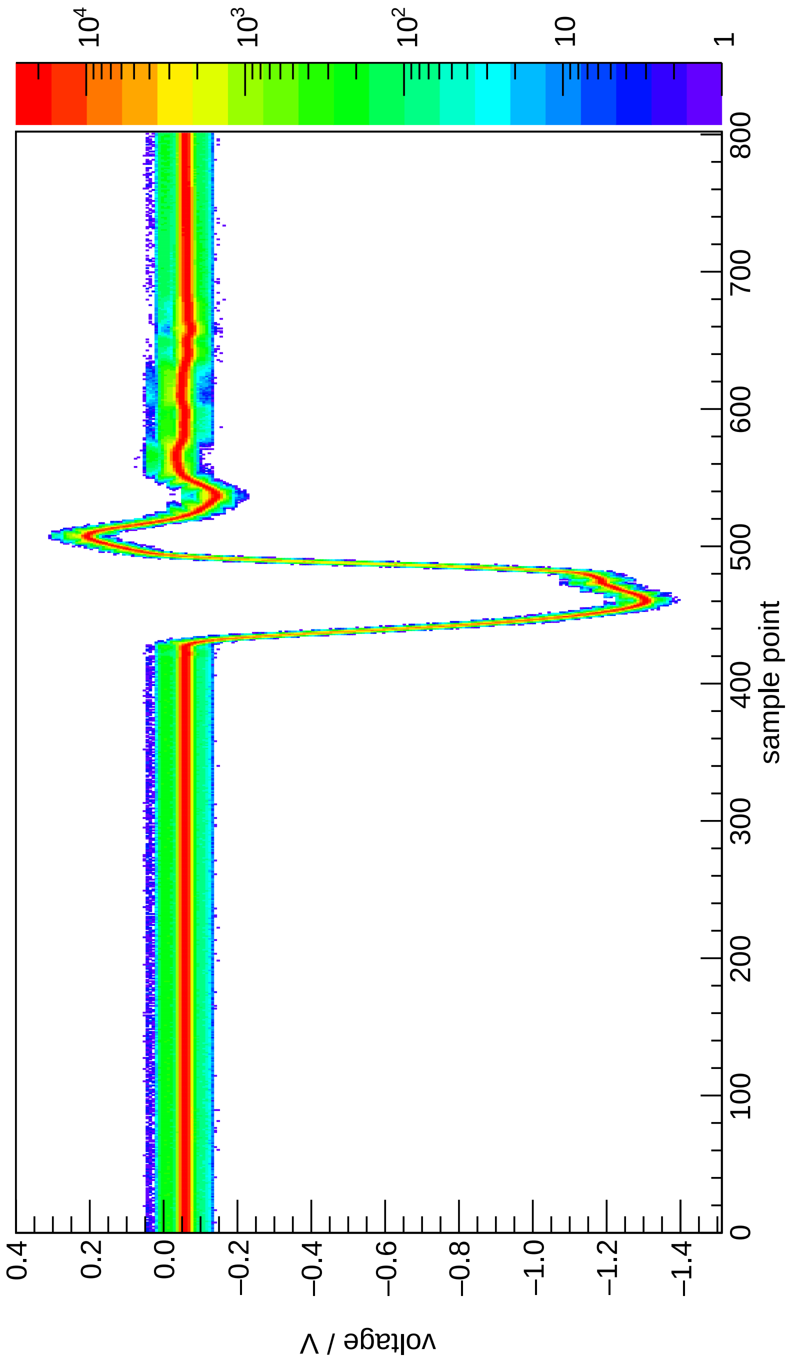

Fig. 6.3.: Example of a histogram of pulses.

A two dimensional histogram, filled with all measured waveforms for DDV = 3334 and PL = 5 is presented. In total, the histogram consists of 71304 waveforms. The pulses are binned in x-direction as sample points (width 1 sample point) and in y-direction in 50 bins in a range of -1.5 V to 0.5 V. The x- and y-axes are linear, the color is presented in a logarithmic scale.

6.4. Baseline

In the first step of the analysis, the baseline is determined. The baseline B is defined as the average value recorded in the first 100 sample points or in mathematical notation as

$$B = \frac{1}{100} \times \sum_{i=0}^{99} s(i)\,. \tag{6.1}$$

This is possible, because the measurement window starts approximately 40 ns before a signal is produced. Due to this, no part of the signal is recorded within the first 100 sample points (corresponding to 12.5 ns) of the waveform. Therefore, the sample points can be used to determine the baseline of the PTC without a signal applied. In Figure 6.4, the baseline as well as a sampled waveform can be seen.

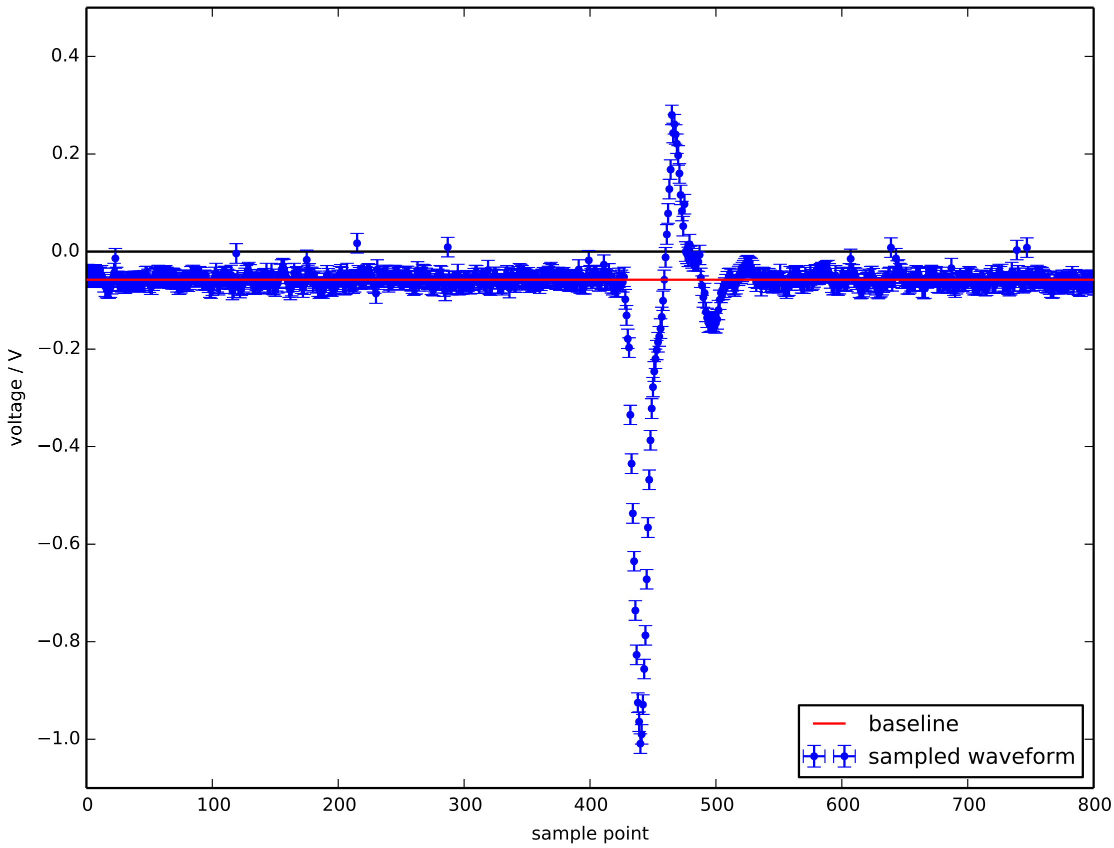

Fig. 6.4.: Waveform, first stage of analysis.
One waveform taken by the measurement system is shown. The baseline, as found by the analysis, is indicated by a red (light), horizontal line. The baseline is restored after the pulse.

6.5. Whittaker–Shannon reconstruction

The Whittaker–Shannon reconstruction is a sinus cardinalis interpolation of a sampled signal to obtain the true analog signal [Whi15]. The Whittaker–Shannon reconstruction is mathematically perfect as long as the sample points are equidistantly spaced and the bandwidth of the signal does not exceed half of the sampling rate (Nyquist frequency).
The Whittaker–Shannon function is defined as

$$f_{\mathrm{WS}}(t) = \sum_{i=-\infty}^{\infty} s(i) \times \mathrm{sinc}\left(\frac{t}{T} - i\right). \tag{6.2}$$

A Whittaker-Shannon reconstruction can be seen in Figure 6.5.

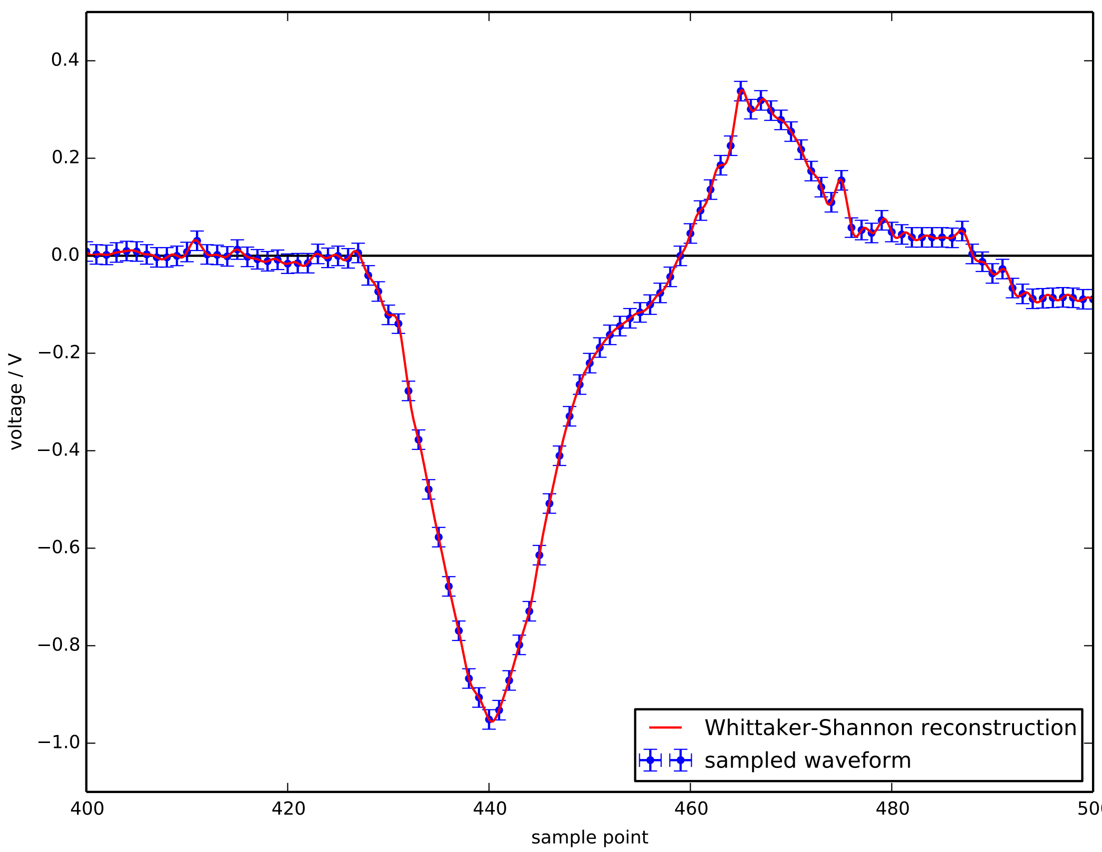

Fig. 6.5.: Sampled waveform with superimposed Whittaker-Shannon reconstruction. In the Figure, a sampled waveform with the corresponding Whittaker-Shannon reconstruction is shown.

6.6. Piecewise linear interpolation

The piecewise linear interpolation connects sampled points with a straight line. This can be described as

$$f_{\mathrm{lin}}(t) = \sum_{i=0}^{I-1} \Theta(t - i \times T) \times \Theta(t - (i+1) \times T) \times \left(s(i) + \frac{s(i+1) - s(i)}{T} \times (t - T \times i) \right) \quad (6.3)$$

where

$$\Theta(x) = \begin{cases} 0 & x < 0 \\ 1 & x \geq 0 \end{cases} \quad (6.4)$$

is the Heaviside function.
While a piecewise linear interpolation is continuous, it is not continuously differentiable. A piecewise linear interpolation can be seen in Figure 6.6.

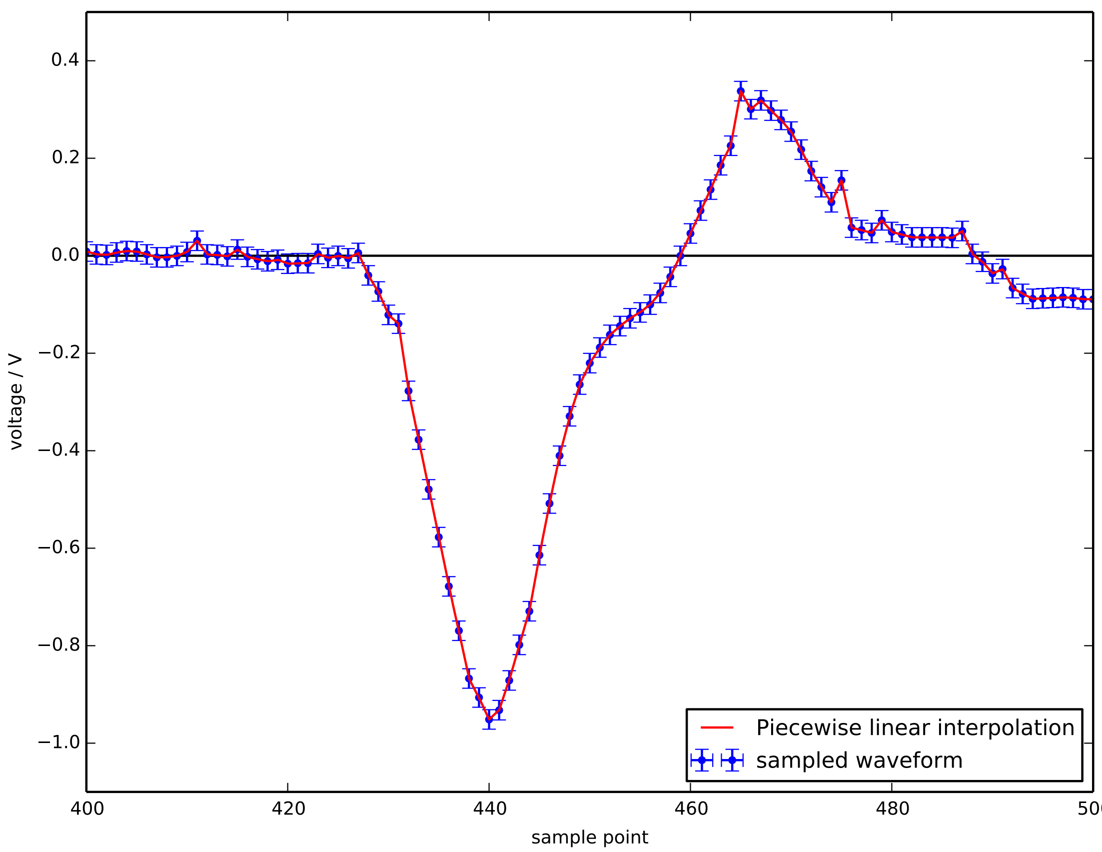

Fig. 6.6.: Sampled waveform with superimposed piecewise linear interpolation. In the Figure, the same sampled waveform as in Figure 6.5 with the corresponding piecewise linear interpolation is shown.

6.7. Waveform characterization parameters

In this analysis, eight parameters are used to characterize the behavior of the waveform. These are called the WCPs. The WCP max is the maximal voltage of the pulse. No attempt is made to compensate for potential overshoots. The second parameter is the position of the peak voltage of the waveform, referenced as pos_max. The next three parameters are the transition points of the waveform through the 10 %, the 50 %, and the 90 % mark of the peak voltage on the rising edge of the waveform. These parameters are called x10p, x50p, and x90p. The last three parameters are defined analogously but are located on the falling edge of the waveform. They are called x10n, x50n, and x90n. If the waveform has multiple transition points for one parameter, the closest location in time to the maximum is selected. In Figure 6.7 the aforementioned parameters are shown with an exemplary waveform.

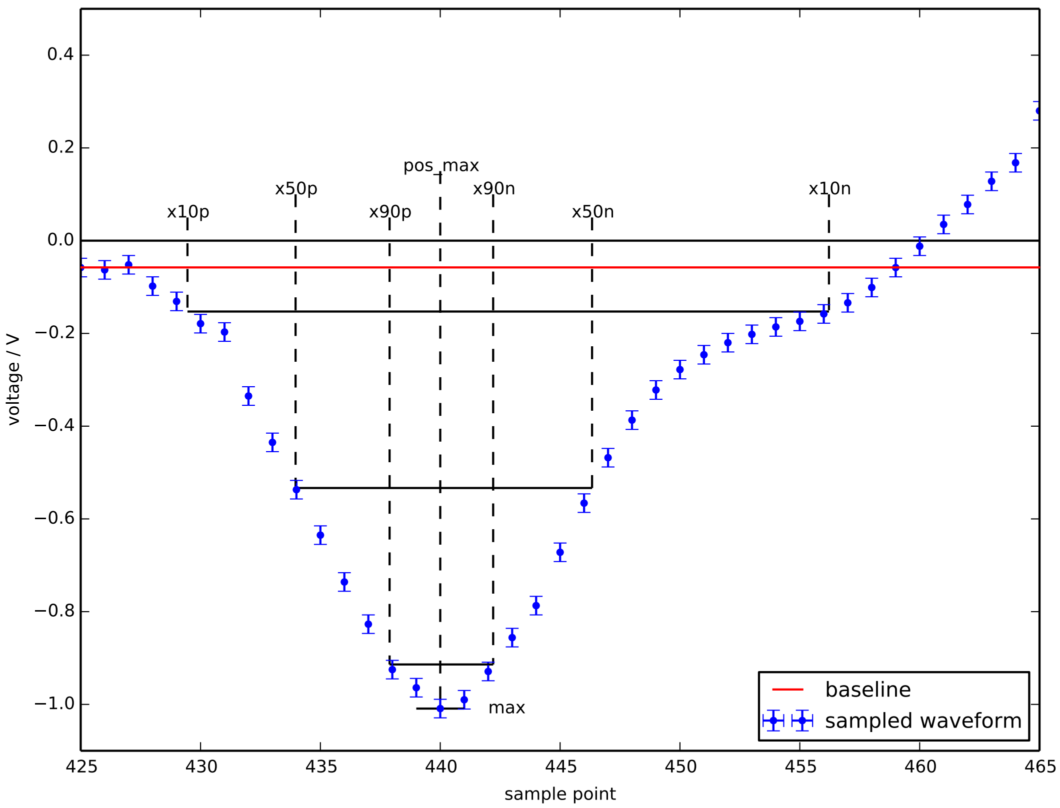

Fig. 6.7.: Parameter extraction.
A part of the waveform seen in Figure 6.4 is shown. The WCPs are indicated. Additionally, horizontal lines at 10 % of the maximum, 50 % of the maximum, and 90 % of the maximum are drawn.

6.8. Combination and analysis

After each waveform has been characterized and the eight WCPs are measured, the individual WCPs of all waveforms with the same WIP are combined. For each WCP, the mean, the root mean square (RMS), and the standard error of mean (SEM) are calculated. The mean,the RMS, and the SEM of a set of values x_i are

$$\langle x \rangle = \frac{1}{N} \times \sum_{i=0}^{N} x_i \,, \tag{6.5}$$

$$\mathrm{RMS}\,(x) = \sqrt[2]{\frac{1}{N} \times \sum_{i=0}^{N} (\langle x \rangle - x_i)^2} \,, \text{ and} \tag{6.6}$$

$$\mathrm{SEM} = \frac{\mathrm{RMS}}{\sqrt{N-1}} \,. \tag{6.7}$$

Figure 6.8 and Figure 6.8 show the distributions of all WCPs for one set of WIPs. Additionally, for each waveform the FWHM is calculated. The FWHM is a function of the WCPs:

$$\mathrm{FWHM}\,(\mathrm{x50n},\, \mathrm{x50p}) = \mathrm{x50n} - \mathrm{x50p} \,. \tag{6.8}$$

The mean and the RMS of the distribution of the FWHMs are derived. The distribution of the FWHM is shown for the same set of WIPs in Figure 6.10.

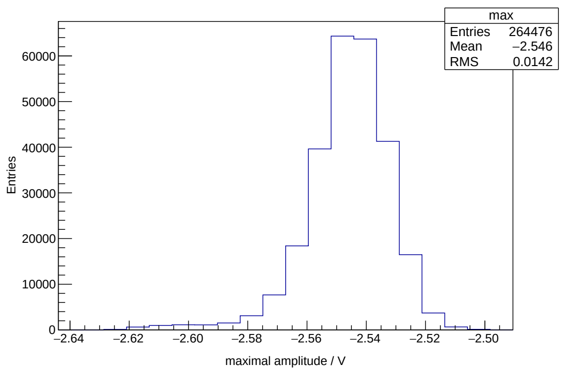

(a) Distribution of WCP max.

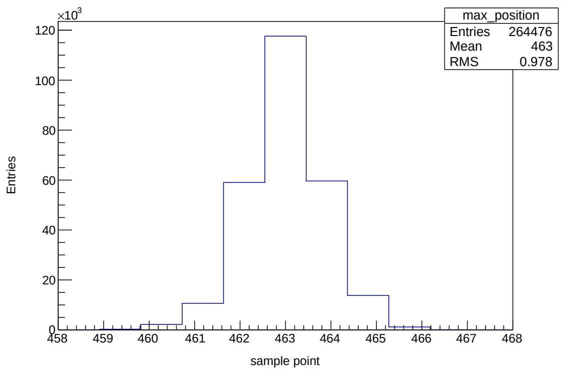

(b) Distribution of WCP pos_max.

Fig. 6.8.: Distribution of the WCPs.
The distributions of all WCPs for a fixed DDV and PL are shown. The DDV is 6660 and the PL is 5 *output clock cycles*.

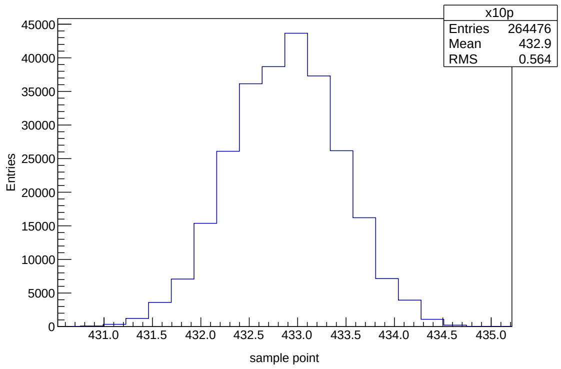

(a) Distribution of WCP x10p.

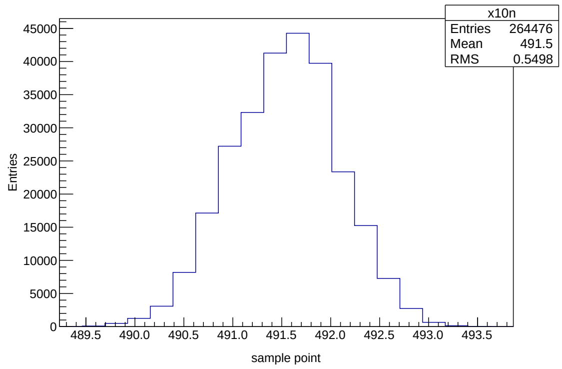

(b) Distribution of WCP x10n.

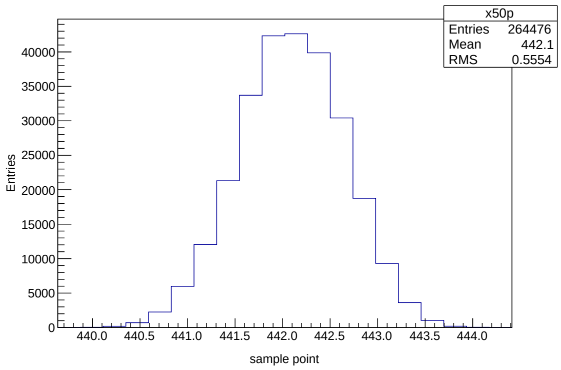

(c) Distribution of WCP x50p.

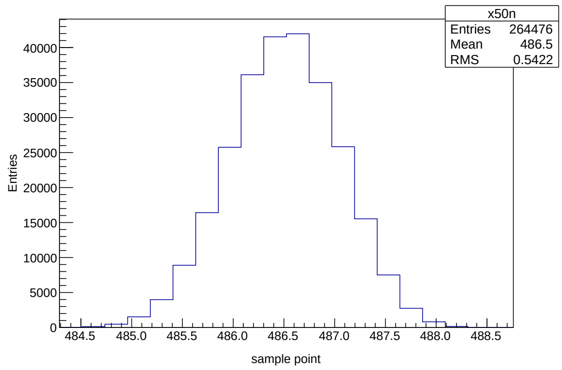

(d) Distribution of WCP x50n.

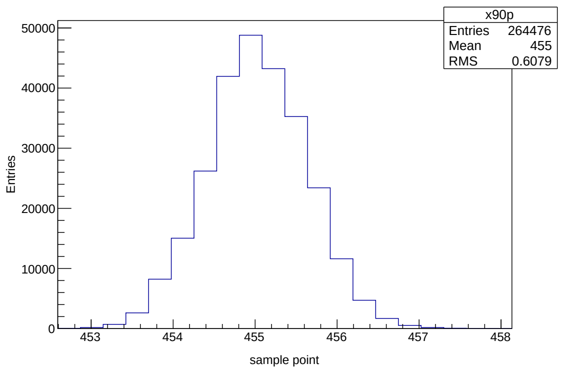

(e) Distribution of WCP x90p.

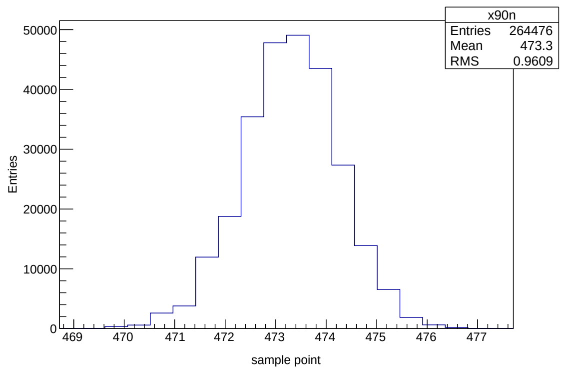

(f) Distribution of WCP x90n.

Fig. 6.9.: Distribution of the WCPs, continued.
The distributions of the all WCPs for a fixed DDV and PL are shown. The DDV is 6660 and the PL is 5 *output clock cycles*.

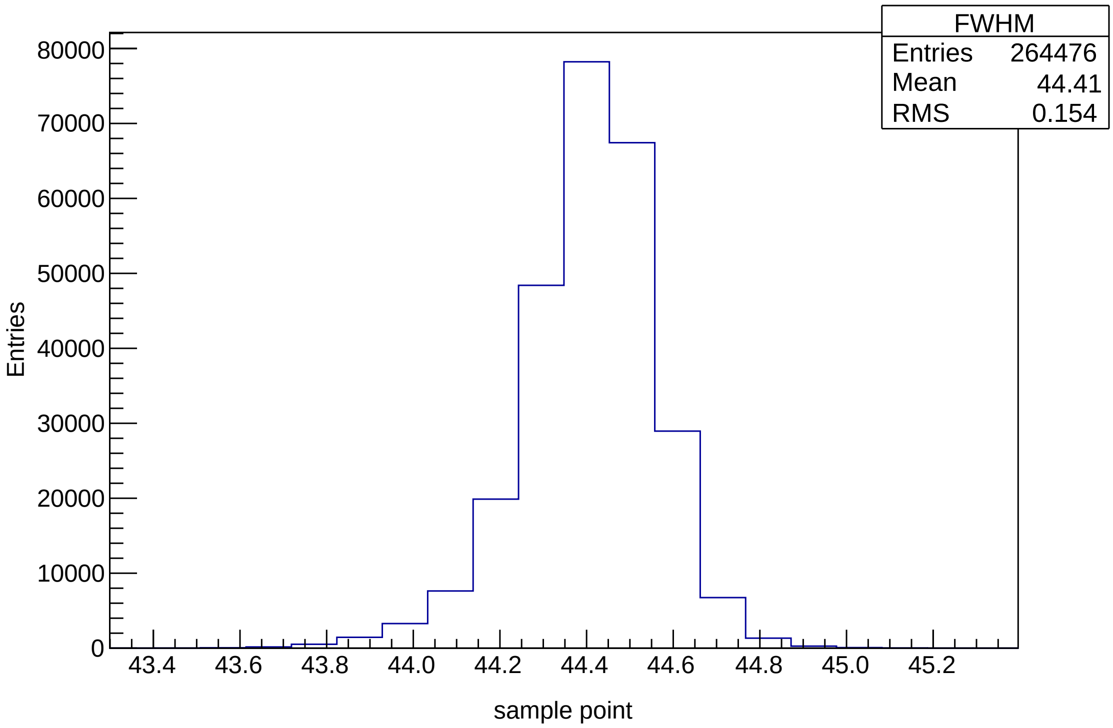

Fig. 6.10.: Distribution of FWHM.
The DDV is 6660 and the PL is 5 *output clock cycles*.

6.8.1. WCPs as a function of the WIPs

The distribution of the means, as a function of one of the two WIPs, PL or DDV, is fitted to a polynomial of the form

$$g(x) = \sum_{i=0}^{N} p_i \times x^i \,. \tag{6.9}$$

The SEM of each parameter is used as a weight for each mean.
Two correlations are of special interest. The first correlation is the connection between the WIP DDV and the WCP max i. e., the programmed and the measure pulse height. A linear correlation is expected. Due to the multiplication factor at the multiplier of the PTC, the constant, inverting amplification factor $K = -2$, and the non normalized second input (1.25 V instead of 1 V) at the second input of the multiplier (see Figure 4.1 and Equation 4.2), the slope of the maximal amplitude as a function of the DDV is expected to be $-2 \times 0.15\,\mathrm{mV} \times \frac{1.25\,\mathrm{V}}{1\,\mathrm{V}} = -0.375\,\mathrm{mV}$.
The second correlation is the correlation between the WIP PL and the FWHM i. e., the programmed and measured pulse width. Using the parameters defined before, FWHM is x50n − x50p. A one-to-one correlation is expected. As the FWHM is expressed in units of

sample points (125 ps) and the PL is expressed in units of *output clock cycles* (1.25 ns), a factor of 10 is introduced.
The last expectation is, that the position of the pulses should always be the same as PSD was not altered. Here, the x50p parameter will be used as a qualifier for the position of the pulse as x50p is obtained from the steepest part of the pulse and should be well defined.

6.8.2. χ^2-test

Every independent, measured value has an associated measurement uncertainty and not only a single value will be measured, but a distribution of values. The spread of this distribution is connected to the measurement uncertainty of the value.
The χ^2-test [Bie38] is a method to check if the measured distribution of values is compatible with a given hypothesis in the sense, that any difference can be explained by random fluctuations within the uncertainty of the measurement. The measured data is split into N classes y_i. The spread within this class, assuming a Gaussian distribution, is called σ_i. In the context of the χ^2-test, χ^2 is the quadratic distance of the hypothesis for a class h_i to the measured data per class y_i normalized to the measurement error σ_i, in mathematical notation

$$\chi^2 = \sum_{i=0}^{N} \left(\frac{y_i - h_i}{\sigma_i} \right)^2 . \tag{6.10}$$

For n independent, Gauss distributed variables, χ^2 follows the χ^2_n-distribution. The probability function of the χ^2_n-distribution is:

$$p_n(\chi^2) = \begin{cases} \frac{\chi^{2\,\frac{n}{2}-1} e^{-\frac{\chi^2}{2}}}{2^{\frac{n}{2}} \Gamma(\frac{n}{2})} & \chi^2 > 0 \\ 0 & \chi^2 \leq 0 \end{cases} \tag{6.11}$$

where n is the number of degree of freedom (NDF). For a polynomial fit, the NDF is the number of classes N minus the count of fitted parameters g [ASM10]. Hence,

$$\mathrm{NDF} = N - g. \tag{6.12}$$

The Γ function is equal to

$$\Gamma(x) = (x-1)!\,. \tag{6.13}$$

The probability, that the hypothesis is compatible with the measured data, can then be calculated by

$$P\left(x \leq \chi^2\right) = 1 - \frac{\int_{\chi^2}^{\infty} p_n(x)\,dx}{\int_{-\infty}^{\infty} p_n(x)\,dx}. \tag{6.14}$$

6.8.3. Maximal signal amplitude as a function of the DDV

To investigate the correlation between the DDV and the measured maximal signal amplitude, the mean and the SEM of the WCP max, seen in 6.8a, as a function of the DDV have been plotted in a diagram. For each PL, a separate diagram is generated and a polynomial fit of the order 1 is performed. Two examples are presented in Figure 6.11 and Figure 6.12. Figure 6.13 shows a zoomed in part of Figure 6.12 with the different uncertainties due to the different measurement counts. The linear fit is subjected to a χ^2 test. The χ^2 test rejects the expected linear model. The polynomial fit of order 2 is performed and subjected to a χ^2 test. The χ^2 test also rejects the quadratic model. This indicates, that both fit models used are not sufficient to explain the data. While the models do not describe the data perfectly well, they can be used as an approximation. The maximum, absolute difference between the data and the fit is 80 mV for the linear fit model and 40 mV for the quadratic fit model. The mean, absolute difference between the data and the fit is 11 mV for the linear fit model and 4 mV for the quadratic fit model. This is mainly due to the lower region of the data.. If only the region above DDV > 400 is taken into account, the maximum, absolute difference between the data and the fit drops to 30 mV for the linear fit model and to 16 mV for the quadratic fit model. The fitted parameters become independent for PL ≥ 4 *output clock cycles*. Table 6.1 shows the mean fit parameters in this region. The fit parameters, as a function of the PL for the polynomial fit of order 1 are shown in Figure 6.14, Figure 6.15. The fit parameters, as a function of the PL for the polynomial fit of order 2 are shown in Figure 6.17, Figure 6.18, and Figure 6.19.

order	$\langle p_2 \rangle$ /nV	$\langle p_1 \rangle$ /mV	$\langle p_0 \rangle$ /mV
1	/	-0.381635 ± 0.000003	8.51 ± 0.01
2	-2.5116 ± 0.0005	-0.343161 ± 0.000004	-31.808 ± 0.006

Tab. 6.1.: Mean fit parameters for PL ≥ 4.
A table with the mean fit parameters describing the correlation between the DDV and the measured maximal amplitude for PL ≥ 4 is shown. p_N is the factor for the N^{th} potent term of the fitted polynomial.

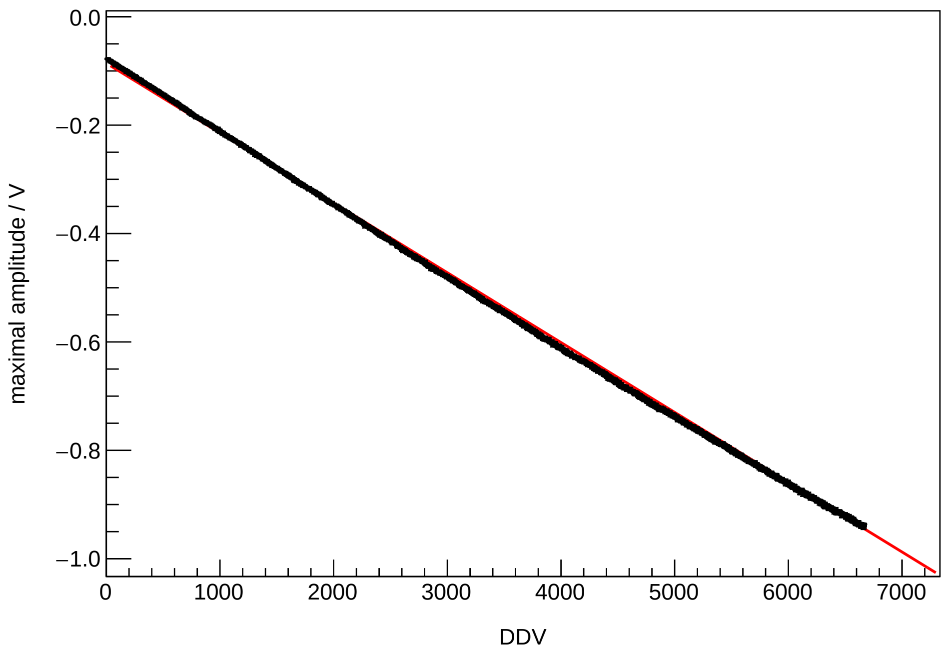

Fig. 6.11.: Exemplary fit for PL $=1$, polynomial order 1.
The data points with error bars are drawn in black, the fit is drawn in red (gray)

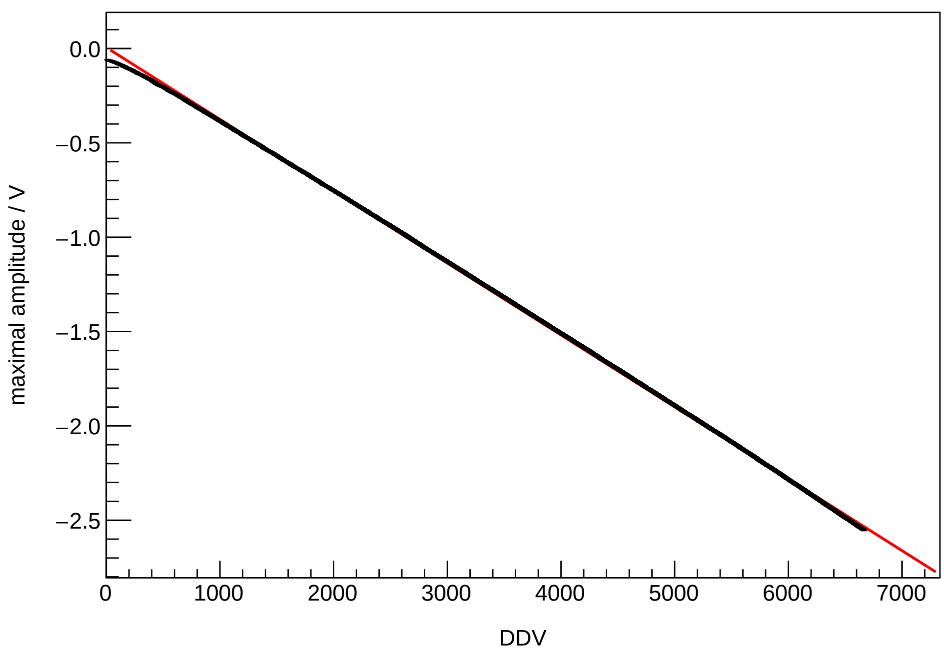

Fig. 6.12.: Exemplary fit for PL $=5$, polynomial order 1.
The data points with error bars are drawn in black, the fit is drawn in red (gray)

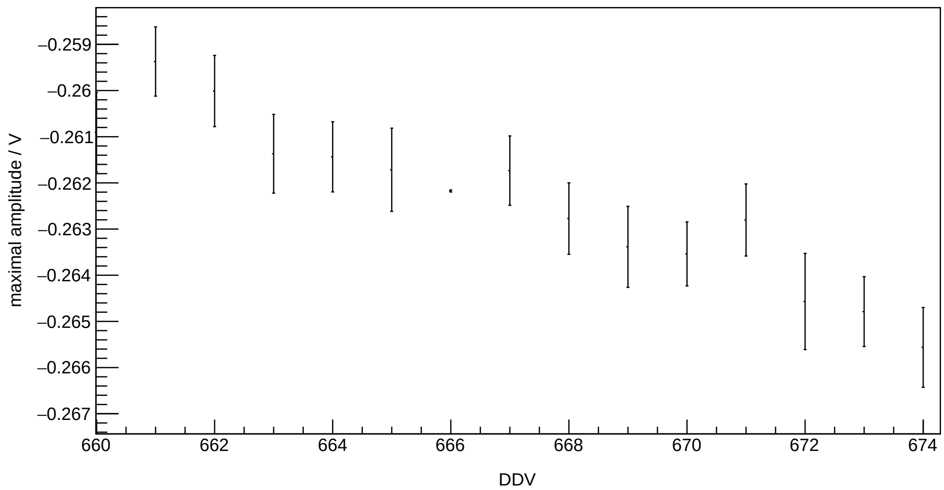

Fig. 6.13.: Enlarged view of the data for PL $= 5$.
The figure shows the calculated SEM for low and high statistics measurements. The uncertainty of the high statistics measurement (DDV $= 666$) is $\approx \frac{1}{40}$ of the uncertainty of the low statistics measurements.

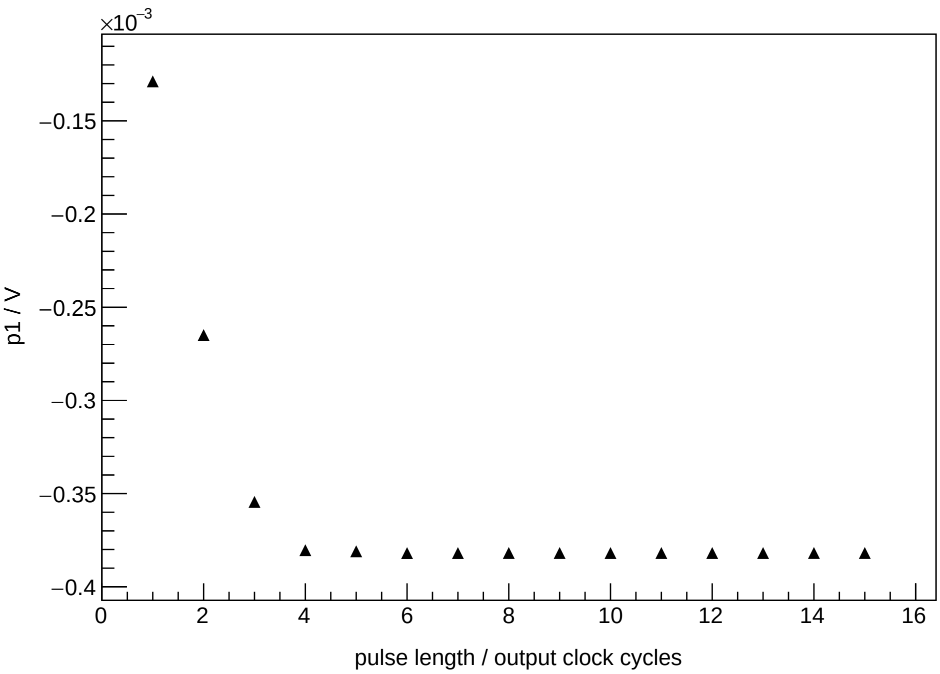

Fig. 6.14.: Fit parameter p_1 as a function of PL, polynomial order 1.
Error bars are included but too small to see.

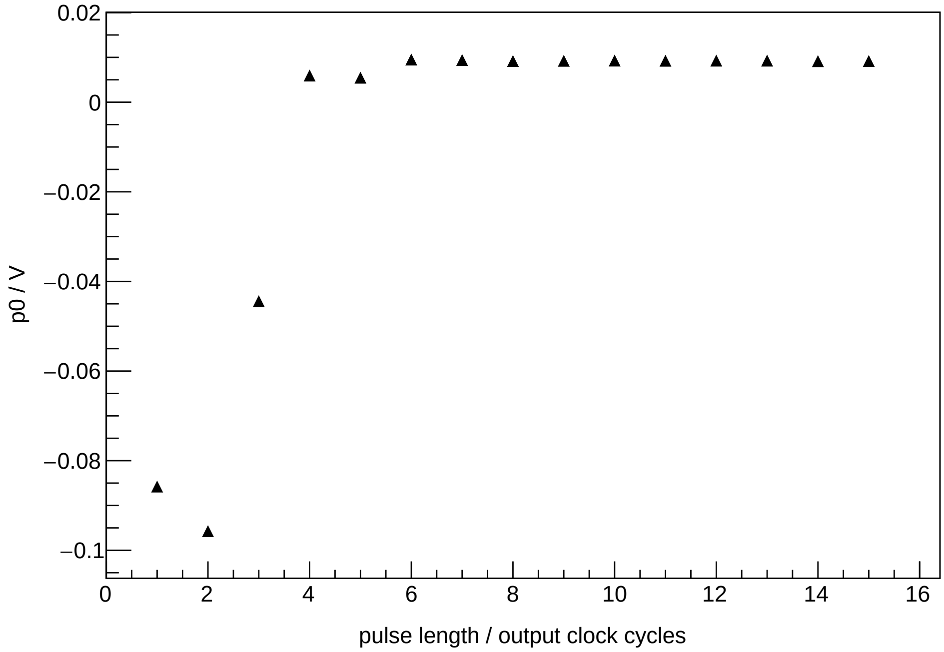

Fig. 6.15.: Fit parameter p_0 as a function of PL, polynomial order 1.
Error bars are included but too small to see.

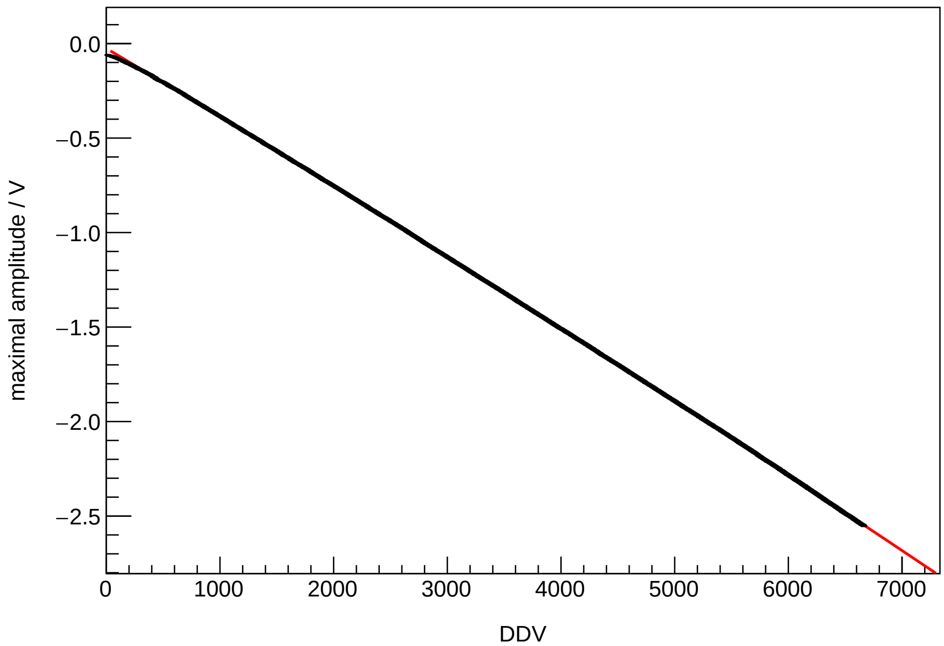

Fig. 6.16.: Exemplary fit for PL = 5, polynomial order 2.
The data points with error bars are drawn in black, the fit is drawn in red (gray)

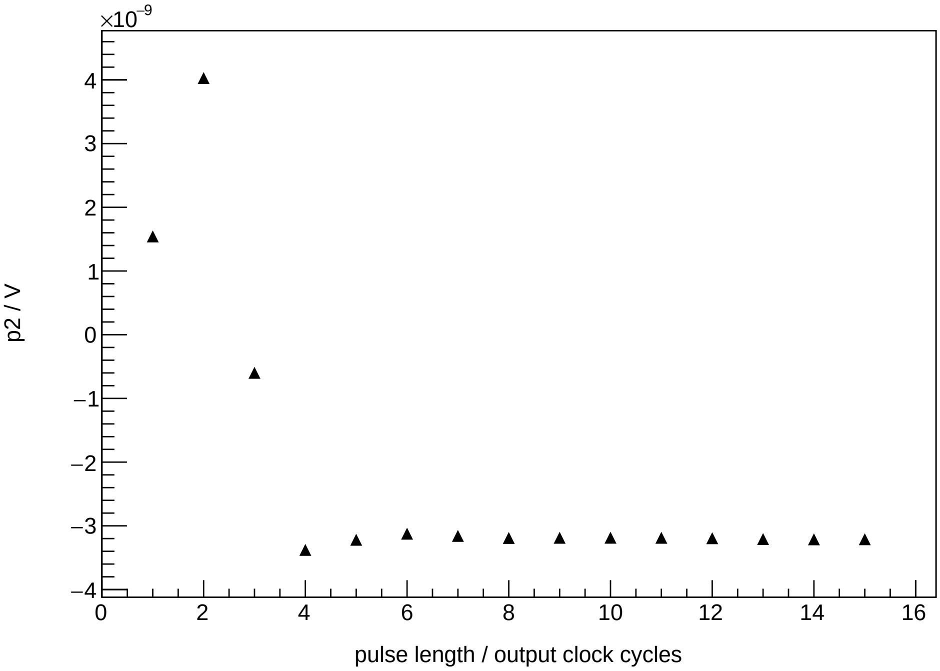

Fig. 6.17.: Fit parameter p_2 as a function of PL, polynomial order 2.
Error bars are included but too small to see.

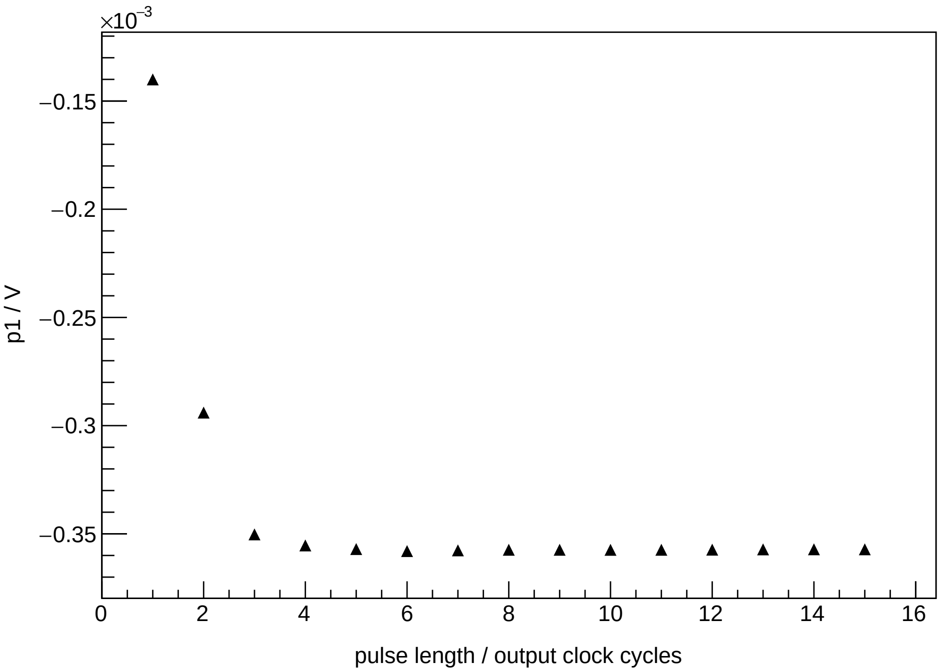

Fig. 6.18.: Fit parameter p_1 as a function of PL, polynomial order 2.
Error bars are included but too small to see.

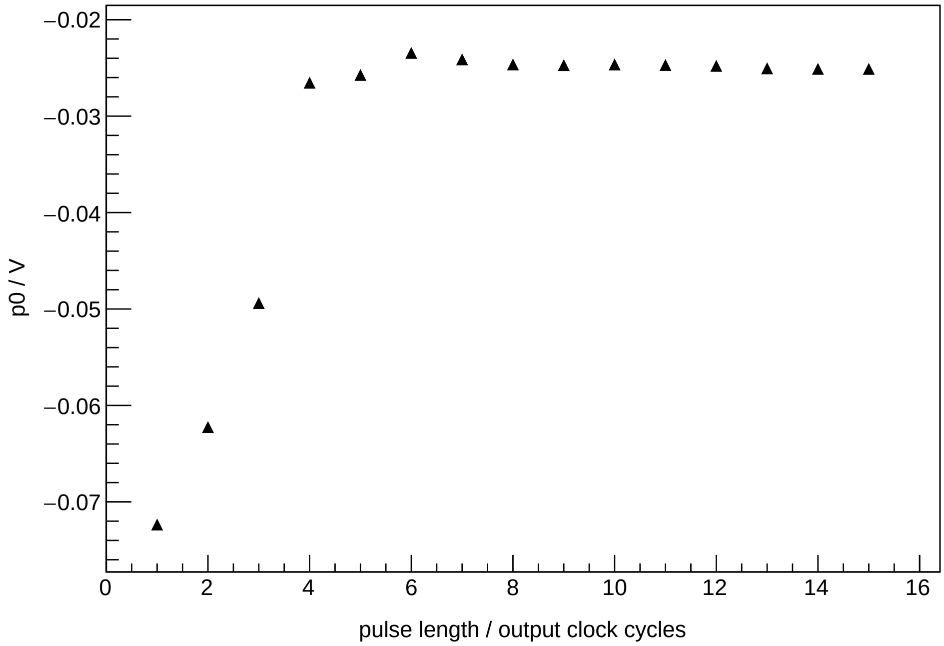

Fig. 6.19.: Fit parameter p_0 as a function of PL, polynomial order 2.
Error bars are included but too small to see.

6.8.4. FWHM as a function of the PL

To investigate the correlation between the measured FWHM and the PL, the mean and the SEM of the FWHM, as seen in Figure 6.10, are plotted in a diagram. For each diagram, a polynomial fit of order 1 is performed. Figure 6.20 and Figure 6.21 show two examples of such diagrams. The linear fits are subjected to a χ^2 test. The χ^2 test rejects the linear fit model. The fit parameters as a function of the DDV is shown in Figure 6.22 and Figure 6.24. The fit parameters become independent of the DDV for $\text{DDV} > 600$. Table 6.2 shows the weighted means of the fit parameters in this region. The expected value of p_1 was 10.
The fit parameters do not converge monotonically but peak in the $250 < \text{DDV} < 400$ region. To determine if this peak is due to a overshoot of the waveform, a new WCP is introduced. This parameter is called x50n_right. x50n_right is the 50 % transition position, just like x50n, but is the most distant point from the maximum. The analysis process for the FWHM is repeated but with $\text{FWHM} = \text{x50n\_right} - \text{x50p}$. If this peak is caused by distortion in the waveform, x50n and x50n_right will have different characteristics. x50n would be positioned left of the distortion, x50n_right would be positioned right of the distortion. If the peaks are not the result of a distortion of the waveform, x50n and x50n_right should be exactly the same and no difference is seen. The resulting diagrams can be seen in Figure 6.23 and Figure 6.25. The peak is less distinct but still detected. Its position is shifted from

$\mathrm{DDV} = 315$ to $\mathrm{DDV} = 340$. This indicates, that the peak is introduced due to a distortion of the form of the signal. Figure 6.26, Figure 6.28, Figure 6.27, and Figure 6.29 show the region of the peak.
The maximum, absolute difference between the linear fits, both for x50n and x50_right, is below 600 ps in the $\mathrm{DDV} \geq 600$ region.

parameter used	$\langle p_1 \rangle$	$\langle p_0 \rangle$
x50n	9.87017 ± 0.00006	-3.794275 ± 0.000007
x50n_right	9.87024 ± 0.00006	-3.796532 ± 0.000007

Tab. 6.2.: Mean fit parameters for $\mathbf{DDV} \geq 600$.
A table with the mean fit parameters describing the correlation between the PL and the measured FWHM for $\mathrm{DDV} \geq 600$ is shown for two different definitions of FWHM. p_N is the factor for the N^{th} potent term of the fitted polynomial and is states in units of $^{\text{sample point}}/_{\textit{output clock cycle}}$.

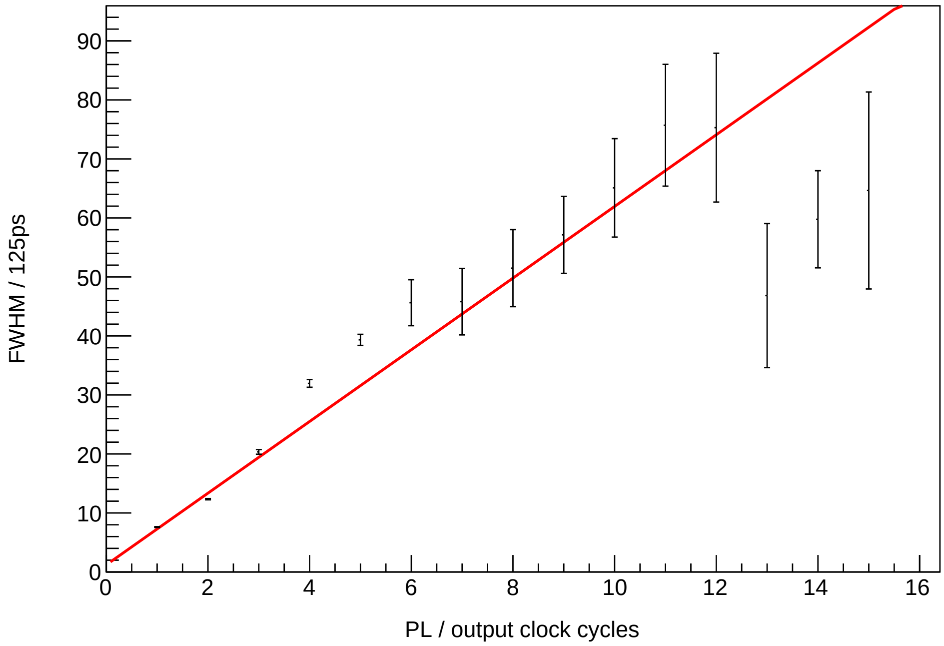

Fig. 6.20.: Exemplary fit for DDV $= 333$.
The data points with error bars are drawn in black, the fit is drawn in red (gray)

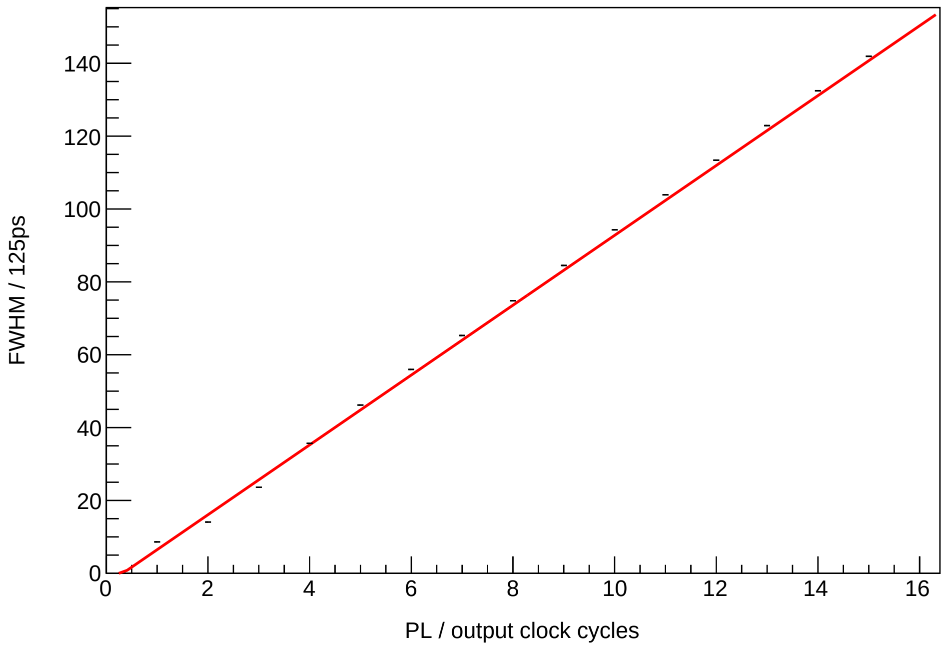

Fig. 6.21.: Exemplary fit for DDV $= 666$.
The data points with error bars are drawn in black, the fit is drawn in red (gray)

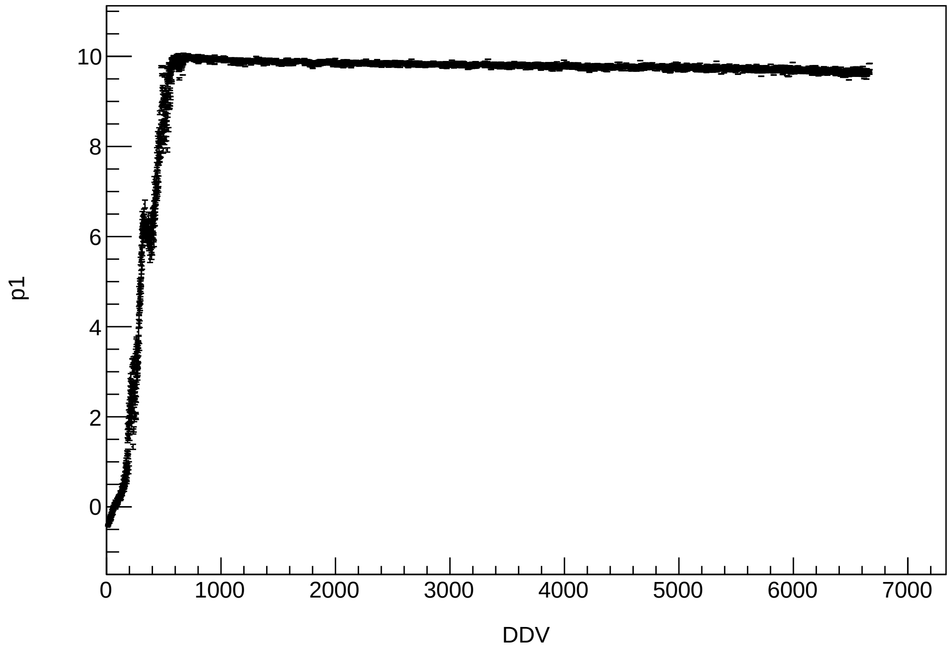

Fig. 6.22.: Fit parameter p_1 as a function of DDV using x50n.
Error bars are included but too small to see.

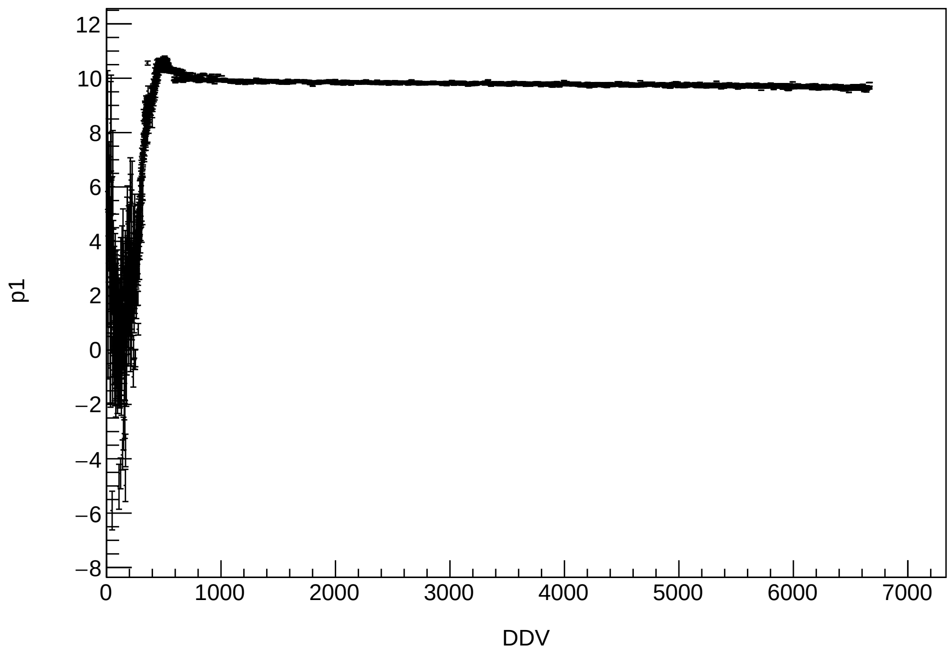

Fig. 6.23.: Fit parameter p_1 as a function of DDV using x50n_right.
Error bars are included but too small to see.

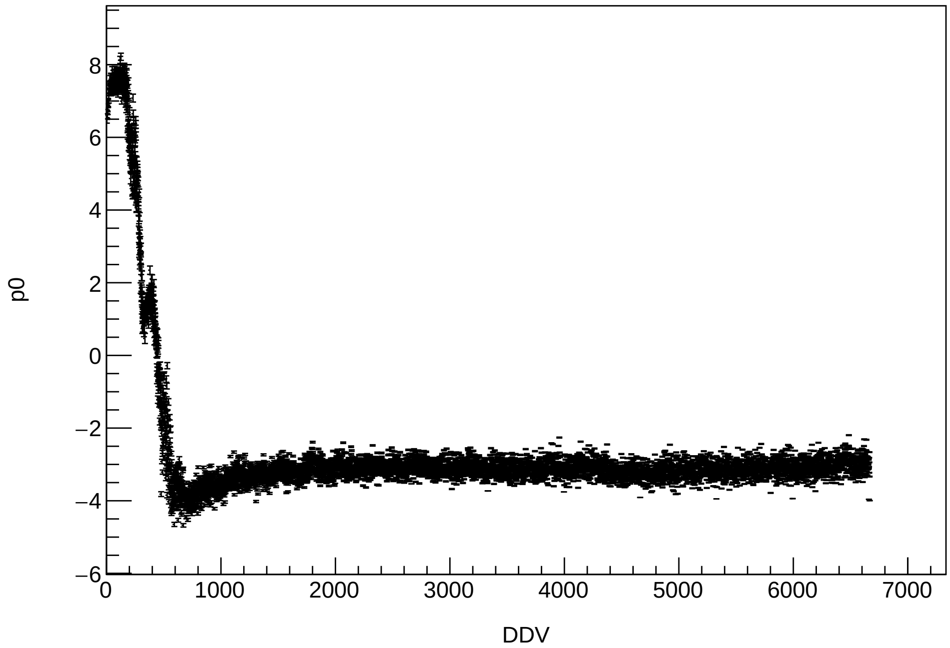

Fig. 6.24.: Fit parameter p_0 as a function of DDV using x50n.
Error bars are included but too small to see.

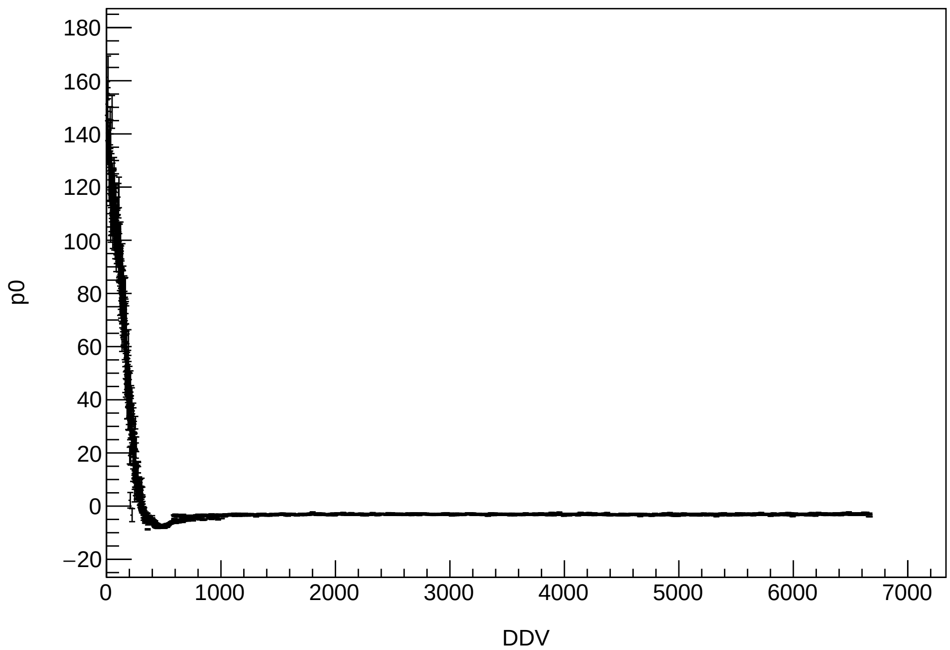

Fig. 6.25.: Fit parameter p_0 as a function of DDV using x50n_right.
Error bars are included but too small to see.

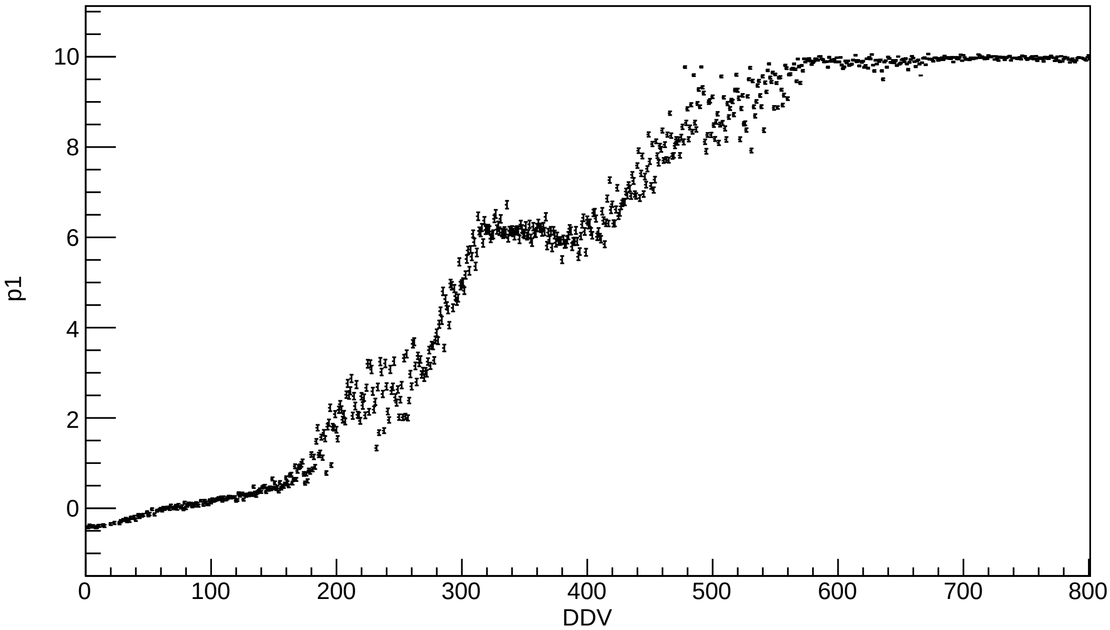

Fig. 6.26.: Fit parameter p_1 as a function of DDV in the $0 \leq$ DDV ≤ 800 region using x50n.

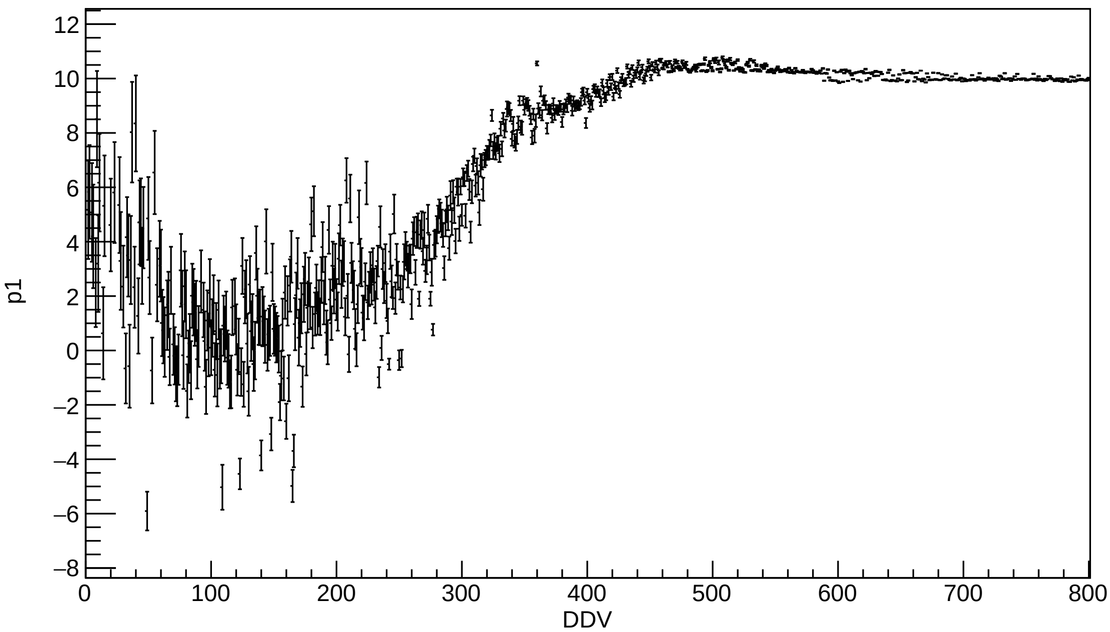

Fig. 6.27.: Fit parameter p_1 as a function of DDV in the $0 \leq$ DDV ≤ 800 region using x50n_right.

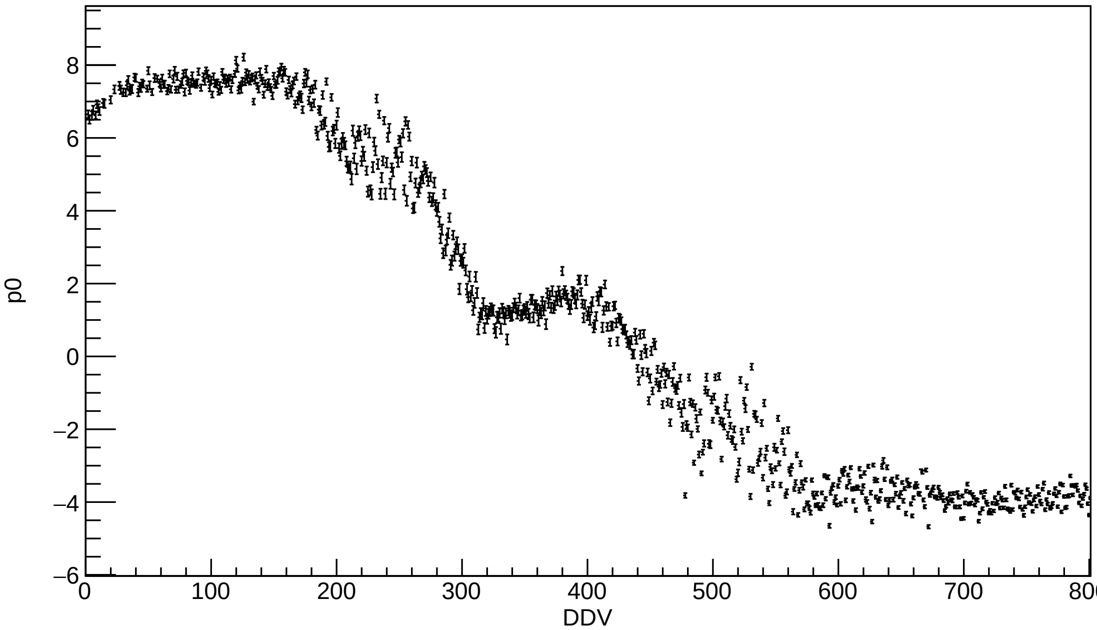

Fig. 6.28.: Fit parameter p_0 as a function of DDV in the $0 \leq$ DDV ≤ 800 region using x50n.

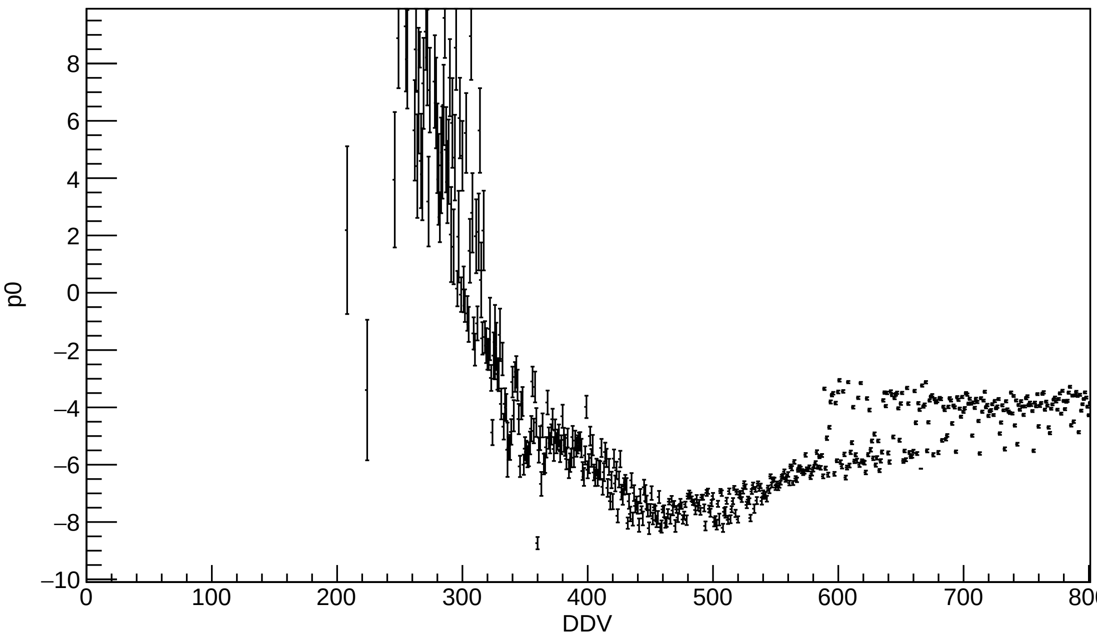

Fig. 6.29.: Fit parameter p_0 as a function of DDV in the $0 \leq$ DDV ≤ 800 region using x50n_right.

6.8.5. Position of the waveform as a function of the PL and DDV

To investigate the relative time shift between two channels of the PTC, the correlation between the position of the waveform and the WIPs needs to be explored. As PSD was always 0, the expectation is that the position of the pulse is always the same within the measurement error. As a marker for the time position of the pulse, x50p is used. Figure 6.30 shows the $\langle$x50p$\rangle$ as a function of the DDV and PL. For $\mathrm{PL} \geq 3$ and $\mathrm{DDV} \geq 600$, $\langle$x50p$\rangle$ is constant at 440 ± 0.5.

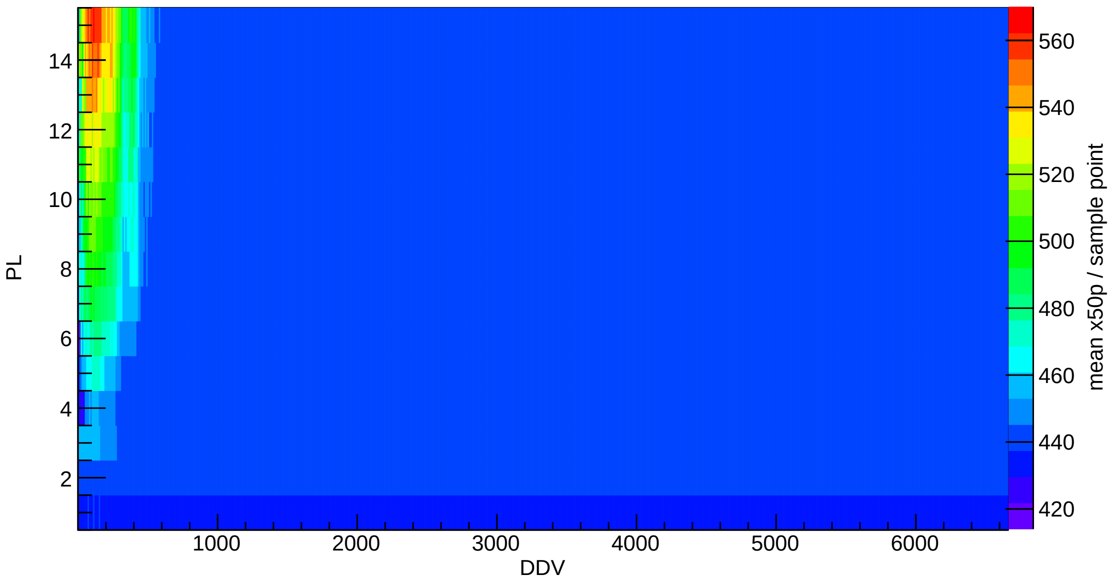

Fig. 6.30.: x50p as a function of DDV and PL.
A histogram with the mean value of the x50p as a function of the DDV and PL is presented. x50p is presented in units of sample points which correspond to 125 ps. Three main regions can be seen. The first region is $\mathrm{DDV} < 600$. Here, $\langle$x50p$\rangle$ fluctuates and is 443 to 480. The second region is $\mathrm{PL} \leq 2$. $\langle$x50p$\rangle$ fluctuates between 434 and 439. The last region is $\mathrm{PL} > 3$ and $\mathrm{DDV} \geq 600$. Here, $\langle$x50p$\rangle$ is constant at 440 ± 0.5.

7 Conclusion

With the completion of this thesis, the following results are achieved:

- An automated measurement system (AMS) for the analog output of the Tank Simulator (TS) of the Pierre Auger Observatory was set up (chapter 5).

- The data acquisition software (DAS) for the AMS was written and tested (section 5.2).

- The necessary Very High Speed Integrated Circuit Hardware Description Language (VHDL) code used by the prototype card of the multiplier method (PTC) was written and tested (subsection 4.2.2).

- Using the recorded data ($\approx$ 65 million waveforms) from the PTC, the performance of one channel of the PTC was analyzed in detail (chapter 6).

7.1. Results

The performance of the first channel of the PTC was tested with high statistics to ensure that the results are not statistically limited. The complete range of digital DAC (digital analog converter) values (DDVs) and pulse lengths (PLs) has been scanned.
The emulated analog output signals of the PTC are characterized by eight waveform characterization parameters (WCPs). These WCPs are combined into two variables, the mean maximal amplitude and the mean full width half maximum (FWHM). A polynomial model is used to describe the mean maximal amplitude and the mean FWHM as a function of the DDV and PL respectively. Limits for the validity of both functions were derived.

The mean maximal amplitude in mV can be described by

$$\begin{aligned}\langle\max\rangle(\mathrm{DDV}) = &-(2.5116 \pm 0.0005)\times 10^{-6}\times \mathrm{DDV}^2\\ &-(0.343161 \pm 0.000004)\times \mathrm{DDV}\\ &-31.808 \pm 0.006\,.\end{aligned} \tag{7.1}$$

The function for the maximal amplitude is valid for $\mathrm{PL} \geq 4$. The maximum, absolute difference between the function and the data is 40 mV. If the DDV range is limited to $\mathrm{DDV} > 400$, the maximal absolute difference is 16 mV.
The mean FWHM in units of sample points (125 ps) can be described by

$$\langle\mathrm{FWHM}\rangle(\mathrm{PL}) = (9.87017 \pm 0.00006)\times \mathrm{PL} - 3.794275 \pm 0.000007. \tag{7.2}$$

The function for the mean FWHM is valid for $\mathrm{DDV} \geq 450$.
The maximum, absolute difference between the function and the data is 600 ps.
The time uncertainty between channel 1 (signal channel) and channel 2 (trigger channel) has been measured. For $\mathrm{PL} > 3$ and $\mathrm{DDV} \geq 600$, the time uncertainty is half a sampling point. This is also the time uncertainty of the AMS. Hence, the time uncertainty between channel 1 and channel 2 is 0.5 ± 0.5 sample points.
In conclusion the PTC should only be used for a $\mathrm{DDV} \geq 600$, which corresponds to a amplitude below -238 mV, and for a $\mathrm{PL} \geq 4$, which corresponds to a FWHM above 3.5 ns.

7.2. Outlook

Voltage precision

To achieve a more precise results with the current equipment used for the AMS, a different measurement technique can be employed. The oscilloscope used for the measurements has a 1 % precision over the full range. Therefore the full range is the limiting factor for a voltage measurement. Instead of measuring high and low amplitude pulses using the same full range, the full range could be adjusted to the maximal amplitude of the waveform. This would limit measurements to waveforms with similar maximal amplitude or would require that the full range is changed for every waveform but would result in a better amplitude precision.

FWHM

Instead of using the WCPs, every single waveform could be fitted to a model describing the waveform. This model would need to include the observed overshoots (see section 6.2). The resulting values for the FWHM should be more precise as the influence of the overshoots on the measured FWHM should be smaller. For details, refer to subsection 6.8.4. In a future version of the PTC the overshoots should be significantly reduced.

Time uncertainty

With the current equipment used for the AMS the maximal precision is achieved, since the result for the time uncertainty between channel 1 and channel 2 of the PTC has the same size as the resolution of the sampling.

A Acronyms

ADC	analog digital converter
AMS	automated measurement system
ASCII	Auger Scintillators for Composition II
CDAS	Central Data Acquisition System
CLK	clock
$\overline{\textbf{CS}}$	inverted chip select
DAC	digital analog converter
DAS	data acquisition software
DDV	digital DAC value
DIN	data in
FD	Fluorescence Detector
FDIR	Failure Detection, Isolation, and Recovery
FMC	FPGA Mezzanine Card
FPGA	field programmable gate array
FWHM	full width half maximum
GPIB	general purpose interface bus
GPS	global positioning system
HEAT	High Elevation Auger Telescopes
ISM	industrial, scientific and medical
JSON	JavaScript object notation
LVCMOS	low voltage complementary metal oxide semiconductor
LZMA	Lempel–Ziv–Markov chain algorithm
NDF	number of degree of freedom
PC	personal computer

PCB	printed circuit board
PL	pulse length
PMT	photomultiplier tube
PN	pulse number
PPC	PowerPC
PSD	pulse start delay
PTC	prototype card of the multiplier method
PULSE	FPGA pulse
RMS	root mean square
SC	Slow Control
SD	Surface Detector Array
SDS	Surface Detector Station
SEM	standard error of mean
SPI	serial peripheral interface
SSD	Surface Scintillator Detector
SU	Subscriber Unit
TAR	tape archiver
TH	Threshold
ToT	Time over Threshold
TS	Tank Simulator
UB	Unified Board
UHECR	Ultra-High-Energy Cosmic Ray
US-ASCII	American standard code for information interchange
USB	universal serial bus
UUB	Upgraded Unified Board
VHDL	Very High Speed Integrated Circuit Hardware Description Language
WCP	waveform characterization parameter
WIP	waveform input parameter

B

Example of a preample

The preample shows the settings used by the oscilloscope for the measurement started at December, 8th, 2014 [Hew02].


```
{   "YOffset":"-1.00000E+00",
    "Max bandwidth":"1.50000E+09",
    "XRange":"1.00000E-07",
    "XOffset":"1.63940000000E-07",
    "YData center":"-1.00000E+00",
    "YData range":"4.26938E+00",
    "Acq mode":"real time",
    "Min bandwidth":"0E+00",
    "Date":"8 DEC 2014",
    "GPIB":"YES",
    "Completion":"100",
    "Count":"1",
    "XOrg":"1.63772616348E-07",
    "Frame":"54845A:US38380131",
    "Coupling":"50 Ohms",
    "XInc":"1.25000000E-10",
    "Points":"804",
    "Y Units":"Volt",
    "Type":"raw",
    "X Units":"second",
    "XRef":"0",
    "Time":"10:19:50:93",
    "YRange":"4.00000E+00"}
```

Bibliography

[Aab+14a] A Aab et al. "Depth of maximum of air-shower profiles at the Pierre Auger Observatory. I. Measurements at energies above $10^{17.8}$ eV". In: *Physical Review D* 90.12 (2014), p. 122005. URL: http://arxiv.org/pdf/1409.4809.

[Aab+14b] A Aab et al. "Probing the radio emission from air showers with polarization measurements". In: *Physical Review D* 89.5 (2014), p. 052002. URL: http://arxiv.org/pdf/1402.3677.

[Abr+10a] J Abraham et al. "The fluorescence detector of the Pierre Auger Observatory". In: *Nuclear Instruments and Methods in Physics Research Section A: Accelerators, Spectrometers, Detectors and Associated Equipment* 620.2 (2010), pp. 227–251. URL: http://arxiv.org/pdf/0907.4282.

[Abr+10b] J Abraham et al. "Trigger and Aperture of the Surface Detector Array of the Pierre Auger Observatory". In: *Nucl. Instrum. Methods A* 613 (Nov. 2010), pp. 29–39. DOI: 10.1016/j.nima.2009.11.018. arXiv: 1111.6764v1 [astro-ph.IM]. URL: http://arxiv.org/pdf/1111.6764v1.

[All+05] D Allard et al. "Aperture calculation of the Pierre Auger Observatory surface detector". In: *arXiv preprint astro-ph/0511104* (2005). URL: http://arxiv.org/pdf/astro-ph/0511104.

[All+08] I Allekotte et al. "The surface detector system of the Pierre Auger Observatory". In: *Nuclear Instruments and Methods in Physics Research Section A: Accelerators, Spectrometers, Detectors and Associated Equipment* 586.3 (2008), pp. 409–420. URL: http://arxiv.org/pdf/0712.2832.

[ASM10] Rene Andrae, Tim Schulze-Hartung, and Peter Melchior. "Dos and don'ts of reduced chi-squared". In: (2010). arXiv: 1012.3754 [astro-ph.IM].

[Bak+10] Keith Baker et al. *ANSI/VITA 57.1 FPGA Mezzanine Card (FMC) Standard*. Tech. rep. ANSI, 2010.

[BEH09] Johannes Blümer, Ralph Engel, and Jörg R Hörandel. "Cosmic rays from the knee to the highest energies". In: *Progress in Particle and Nuclear Physics* 63.2 (2009), pp. 293–338. URL: http://arxiv.org/pdf/0904.0725.

[Ber+14] Ad van den Berg et al. *Final recommendations of the Upgrade Committee*. Tech. rep. Pierre Auger Observatory, 2014.

[Bie38] I. J. Bienayme. "Memoire sur la probabilite des resultats moyens des obseravations; demonstration directe de la regle de Laplace". In: *Series Etrangers* 5 (1838), pp. 513–558.

[Bir+93] DJ Bird et al. "Evidence for correlated changes in the spectrum and composition of cosmic rays at extremely high energies". In: *Physical Review Letters* 71.21 (1993), p. 3401. URL: http://journals.aps.org/prl/abstract/10.1103/PhysRevLett.71.3401.

[Bra14] Ed. T. Bray. *The JavaScript Object Notation (JSON) Data Interchange Format*. Tech. rep. Internet Engineering Task Force, May 2014. URL: http://tools.ietf.org/html/rfc7159.

[Cer69] Vint Cerf. *ASCII format for Network Interchange*. Tech. rep. Internet Engineering Task Force, May 1969. URL: http://tools.ietf.org/html/rfc20.

[Che34] Pavel A. Cherenkov. "Vidimoe svechenie chistyh zhidkostej pod dejstviem γ-radiacii". In: *Doklady Akademii Nauk SSSR* 2 (1934), pp. 451–454.

[Che37] Pavel A. Cherenkov. "Visible radiation produced by electrons moving in a medium with velocities exceeding that of light". In: *Physical Review* 52.4 (1937), p. 378. URL: http://journals.aps.org/pr/abstract/10.1103/PhysRev.52.378.

[Col13] The Pierre Auger Collaboration. *The Next Frontier in UHECR Research with an Upgraded Pierre Auger Observatory*. Sept. 2013. URL: http://arxiv.org/pdf/1307.0226v3.

[Czi] Hendrik Czirr. *Private Communication*.

[Deva] Analog Devices. *AD5620/AD5640/AD5660 Single, 12-/14-/16-Bit nanoDAC with 5 ppm/°C On-Chip Reference in SOT-23*.

[Devb] Analog Devices. *AD835: 250 MHz, Voltage Output, 4-Quadrant Multiplier*.

[Gen+01] B Genolini et al. *Design of the photomultiplier bases for the surface detectors of the Pierre Auger Observatory*. Tech. rep. 2001. URL: http://cds.cern.ch/record/507111.

[Gin40] V. L. Ginzburg. “Quantum theory of light radiation of an electron uniformly moving through a medium”. In: *Zh.Eksp.Teor.Fiz* 10 (1940), pp. 589–600.

[Hew01] Hewlett-Packard. *Service Guide, Agilent Model 54845A*. 2001.

[Hew02] Hewlett-Packard. *Programmer’s Reference*. Mar. 2002.

[JED07] JEDEC. *JESD8-5A.01, 2.5 V ± 0.2 V (Normal Range) and 1.8 V – 2.7 V (Wide Range) Power Supply Voltage and Interface Standard for Nonterminated Digital Integrated Circuits*. Tech. rep. JEDEC, Sept. 2007.

[KLA07] Hans O KLAGES. “HEAT–Enhancement Telescopes for the Pierre Auger Southern Observatory”. In: *Proc. 30th ICRC, Merida*. 2007. URL: http://people.na.infn.it/~valore/pubblicazioni/articoli/C.C.40.pdf.

[Kol] Yury Kolotaev. *Private communication*.

[KV14] Yury Kolotaev and Marco Vogt. *Analog Test Board, v.3.00.2014.08*. University Siegen, Aug. 2014.

[Oli+14] K.A. Olive et al. “Review of Particle Physics”. In: *Chin.Phys.* C38 (2014). DOI: 10.1088/1674-1137/38/9/090001.

[Pro15] Pierre Auger Project. *Surface Detector Station #358*. Mar. 2015. URL: https://auger.ikp.kit.edu/photos/photo_archive2/DSC00358.tif.

[RS12] H Rebel and O Sima. “INFORMATION ABOUT HIGH-ENERGY HADRONIC INTERACTION PROCESSES FROM EXTENSIVE AIR SHOWER OBSERVATIONS”. In: *ROMANIAN JOURNAL OF PHYSICS* 57.1-2 (2012), pp. 472–492. URL: http://www.nipne.ro/rjp/2012_57_1-2/0472_0492.pdf.

[Set11] Mariangela Settimo. “An update on a search for ultra-high energy photons using the Pierre Auger Observatory”. In: *The Pierre Auger Observatory III: Other Astrophysi-cal Observations* (2011), p. 17. URL: http://arxiv.org/pdf/1107.4805#page=22.

[Spa08] R Sparvioli. “Direct measurements of cosmic rays”. In: *Nuovo Cimento della Societa Italiana di Fisica. B, General Physics, Relativity, Astronomy and Mathematical Physics and Methods* 123 (June 2008), pp. 908–911. ISSN: 1594-9982. URL: https://inis.iaea.org/search/search.aspx?orig_q=RN:41088089.

[Sta14] P. Stassi. *Surface Detector Electronics Upgrade UUB Electrical Interface Control Document (EICD)*. Tech. rep. Local Reference: ATRIUM-2223, Project Reference: WP10-LPSC-05E. Pierre Auger Observatory, Nov. 2014.

[Sta15] P. Stassi. *Surface Detector Electronics Upgrade AIT- AIV Plan*. Tech. rep. Local Reference: ATRIUM-4404, Project Reference: WP10-LPSC-11E. Pierre Auger Observatory, 2015.

[Tay08] Frank E. Taylor. *Comparison of cosmic ray flux at* $\sqrt{s} \geq 14$ *TeV with LHC luminosity*. May 2008. arXiv: `0805.4528v1 [hep-ex]`. URL: `http://arxiv.org/pdf/0805.4528v1`.

[TF37] I.E. Tamm and I.M Frank. “Coherent Radiation of Fast Electrons in a Medium”. In: *Doklady Akad. Nauk SSSR* 14 (1937), p. 107.

[Whi15] E. T. Whittaker. “XVIII.—On the Functions which are represented by the Expansions of the Interpolation-Theory”. In: *Proceedings of the Royal Society of Edinburgh* 35 (Jan. 1915), pp. 181–194. ISSN: 0370-1646.

[Xil15] Xilinx. *ZC702 Evaluation Board for the Zynq-7000 XC7Z020 All Programmable SoC User Guide*. Tech. rep. Xilinx, Apr. 2015.

Acknowledgements

I like to thank the High Energy Particle Physics group of Siegen University for my great time as a master student. In particular, I want to thank

- Peter Buchholz, for allowing me to become a member of this group,
- Andreas Tepe, who was a great supervisor, and
- Hendrik Czirr, who helped me a lot by proofreading my thesis.

I also want to thank my family, who made my studies possible in the first place, and my girlfriend, Natalie Wollersheim who helped me during the hardships of writing this thesis.

Thank you all!

Erklärung

Hiermit erkläre ich, dass ich die vorliegende Masterarbeit selbstständig verfasst und keine anderen als die angegebenen Quellen und Hilfsmittel benutzt sowie Zitate und Ergebnisse Anderer kenntlich gemacht habe.

....

(Ort) (Datum) (Unterschrift)